MSc-ma

by Meenakshi Aarushi

Submission date: 26-May-2026 02:29PM (UTC+0530)
Submission ID: 2969730873
File name: 12_50_AM_final_report.docx (26.06M)
Word count: 11625
Character count: 76221

ABSTRACT

Two-dimensional (2D) penta-materials exhibiting inherently buckled structures and often highly degenerate multivalley electronic structures are promising thermoelectric candidates. However, most current computational investigations on these materials treat charge-carrier scattering using analytical models based on continuum approximations. Here, we elucidate the potential importance of an *ab initio* mode-resolved approach to carrier transport for these systems by revisiting the thermoelectric performance of recently predicted penta-Bi_2X (X=Ge,Sn) monolayers. Under acoustic deformation potential theory, these materials when suitably hole- doped were previously reported to yield extraordinary peak ZT values of 7.0 and 5.8 at 700 K. However, our calculations reveal that charge transport in these monolayers is significantly restricted when long-range Fröhlich and intervalley scattering processes are incorporated. Consequently, the predicted peak ZT for p-type Bi_2Ge at 700 K undergoes a substantial correction from 7.0 to 1.0. Conversely, this correction is far less pronounced for p-type Bi_2Sn, which maintains a highly competitive peak ZT of 4.4. This relative robustness is attributed to the notably low lattice thermal conductivity on the order of 10^{-2} W m^{-1} K^{-1} reported in the prior study, which allows a concurrent drop in the electronic thermal conductivity to partially compensate for a heavily decreased electrical conductivity. These insights underscore the importance of advanced scattering models for predicting the performance of non-centrosymmetric materials featuring multiple band and valley degeneracies.

CHAPTER 1: INTRODUCTION

1.1. INTRODUCTION

Thermoelectric (TE) materials are promising candidates for solid-state energy conversion, facilitating the direct conversion of thermal gradients into electrical power via the Seebeck effect [1-2]. Their capacity for efficient waste-heat recovery offers a sustainable path for power generation with the added benefits of mechanical robustness and minimal maintenance requirements [3]. Since a substantial fraction of global energy is dissipated as waste heat, continued efforts toward improving energy conversion efficiency are strongly motivated [1]. An ideal TE material is expected to exhibit a high electrical conductivity (σ) for reduced resistive losses, a high Seebeck coefficient (S) for enhanced voltage generation, and low thermal conductivity (κ) to maintain a sufficient temperature gradient [4]. The most general criterion in determining the conversion efficiency of TE materials is given by the dimensionless figure of merit, $ZT = S^2\sigma T/\kappa$, where T is the absolute temperature in kelvin, and $\kappa = \kappa_{el} + \kappa_{latt}$ is the sum of the electronic thermal conductivity and lattice thermal conductivities. Although a higher ZT value can, in principle, be achieved by either reducing κ or increasing the power factor $PF = S^2\sigma$, the strong interdependence among the S, σ, and κ_{el} makes simultaneous optimization of these parameters quite challenging [5-6]. The common approaches followed so far in enhancing ZT include managing or suppressing intrinsic scattering through optimized electron-phonon coupling (EPC), optimizing carrier concentration, band structure engineering, leveraging quantum confinement effects in low-dimensional, especially 2D systems, to discretize the density of states (DOS), hierarchical phonon scattering, and using materials with strong anharmonicity [7-18].

In high-performance 2D semiconductors, including phosphorene, MoS_2, and Janus PtSSe, electron-phonon interactions (EPI) set the fundamental limits of carrier mobility and thermoelectric performance [19–22]. Traditionally, acoustic deformation potential theory (DPT) has been a primary method for approximating scattering matrix elements due to its

computational efficiency and reliance on macroscopic elastic constants. While DPT effectively models non-polar, isotropic semiconductors with simple, single-valley bands where acoustic phonons dominate, it is inherently limited to the long-wavelength ($q \rightarrow 0$) range of local lattice changes. This local approach does not account for the non-local macroscopic polarization found in polar crystals. For example, in transition metal dichalcogenides (TMDs), out-of-phase longitudinal optical (LO) displacements create long-range electric fields through the Fröhlich interaction, which remains uncaptured within the local DPT framework [23–26]. Moreover, DPT is inadequate for high-performance TE materials that feature valley degeneracy or band convergence. In such complex structures, DPT does not capture the crucial intervalley and interband scattering matrix elements that dominate the electronic phase space. For instance, the misestimation of scattering rates in Sb_2Te_2Se directly results from ignoring intense interpocket optical scattering [25]. This issue is even clearer in buckled honeycomb lattices like stanene, where traditional DPT overestimates mobility by three orders of magnitude (~10^6 vs. ~10^3 $cm^2V^{-1}s^{-1}$) by ignoring essential intervalley ZA and TA scattering [26, 27]. Even in non-polar systems like β-antimonene, where Fröhlich interactions do not exist, including short-range intervalley scattering from optical modes (LO, TO, ZO) provides a contribution comparable to acoustic modes, collectively reducing the predicted electron mobility from $785\ to\ 40\ cm^2V^{-1}s^{-1}$ [28].

Since the theoretical prediction of penta-graphene in 2014, pentagonally tiled 2D materials have attracted attention due to their highly tunable electronic structures under external fields and chemical doping. These materials serve as a promising platform for modifying TE transport coefficients across different monolayer configurations [29]. Unlike the high-symmetry hexagonal lattices of graphene or MoS_2, the broken hexagonal symmetry and complex bonding topology of pentagonal tiling introduce significant structural anisotropy. This reduced symmetry facilitates greater bond-stretching and bond-bending distortions, enhancing phonon-phonon anharmonicity. Consequently, these systems often exhibit suppressed phonon group velocities and significantly reduced phonon lifetimes, leading to the low κ_{latt} desired for high-performance TE materials [30]. For instance, pentagonal monolayers such as penta-GeC_5 and penta-silicene have shown significant TE potential, with ZT values at 300 K of ~2.97 and ~3.4, respectively [31-32]. While the

performance of penta-GeC_5 benefits from high carrier mobility, penta-silicene achieves its ultra-high ZT through a remarkably low κ_{latt} in combination with favorable electronic structure characteristics, such as complicated Fermi surfaces with multiple valley degeneracies and pseudo-flat band edges.

Recently, Lv et al. reported an intrinsic κ_{latt} as low as 0.3 W m^{-1} K^{-1} and 0.03 W m^{-1} K^{-1} at 300 K for penta-Bi_2Ge and penta-Bi_2Sn monolayers, attributing the low κ_{latt} to the anharmonicity arising from the particular buckled structure of 2D penta-materials [33–34]. However, their charge-carrier transport analysis based on acoustic deformation potential theory (DPT) suggested extraordinarily high peak ZT values of 6.96 and 5.79 for optimally hole-doped Bi_2Ge and Bi_2Sn, respectively, at 700 K [34]. However, it should be noted that these non-centrosymmetric penta-monolayers possess polar Bi–X bonds and complex Fermi surfaces characterized by multiple valley degeneracies at the X and M points. Consequently, the acoustic DPT framework fundamentally fails to capture two dominant scattering channels in these systems: (i) the long-range Fröhlich interactions arising from the macroscopic polarization of the lattice [23, 34–35], and (ii) the large-momentum intervalley scattering facilitated by the aforementioned valley degeneracies.

To rigorously address the limitations of the DPT approach, we employ an *ab initio* electron–phonon Wannier (EPW) methodology. Our comprehensive calculations reveal that, in addition to the expected long-range Fröhlich interactions, charge-carrier mobility is severely restricted by large-momentum-transfer intervalley scattering processes that fall completely outside the scope of the Fröhlich model. Furthermore, even for phonons with small but finite crystal momenta, we observe significant corrections driven by short-range perturbations in the crystal potential that are omitted in standard dielectric continuum approximations. Naturally, for Fröhlich-active modes, these deviations become progressively more pronounced as the crystal momentum transfer increases and the system moves away from the Fröhlich singularity.

Moreover, accurately evaluating the electron–phonon coupling strength for acoustic modes and Fröhlich-inactive optical modes requires a full first-principles treatment, as it fundamentally cannot be captured by the Fröhlich formula. A prominent example is the highest-frequency optical phonon branch, which is characterized by counterphase out-of-plane sublattice displacements between the Bi and group-IV atoms. Despite possessing large

off-diagonal elements in the Born effective charge tensor, these modes remain Fröhlich-inactive due to macroscopic cancellation effects. Nevertheless, they constitute some of the most dominant scattering channels for hole-doped Bi_2Ge due to the intense short-range perturbation they exert on the crystal potential. By comprehensively incorporating all such electron–phonon interactions, our work provides a physically complete transport picture. This rigorous treatment reveals a substantial suppression of the previously predicted power factors, establishing advanced, mode-resolved scattering frameworks as indispensable for accurately evaluating the performance limits of complex, non-centrosymmetric 2D networks.

CHAPTER 2: COMPUTATIONAL METHODOLOGY

2.1 COMPUTATIONAL METHODOLOGY

The Density Functional Theory (DFT) [36], electronic structure calculations for penta-Bi_2X (X = Ge, Sn) monolayers were carried out employing the Quantum Espresso (QE) package [37]. To account for core-valence interactions, ONCV pseudopotentials [38] were employed. Exchange-correlation effects were treated using the GGA parameterized by the PBE functional [39]. Additionally, SOC was incorporated at all computational stages, from structural optimization and electronic/phonon calculations through the full electron-phonon Wannier workflow. Consequently, scattering rates and transport properties fully account for the SOC-driven shifts in valley topology, band splitting, and phonon-induced perturbing potentials, which are critical to the scattering phase space in these heavy-atom systems. High converged kinetic-energy cutoffs for the plane wave basis set for the Kohn-Sham wave functions of 50 Ry for Bi_2Sn and 55 Ry for Bi_2Ge monolayers, with corresponding charge-density and electrostatic-potential cutoffs of 200 Ry and 220 Ry, respectively were employed to ensure accurate calculations. The ground state electronic structure and structural relaxations were performed using converged Monkhorst-Pack 8×8×1 k-meshes. To prevent interlayer interactions, a large vacuum spacing of 20 Å was applied along the non-periodic (out-of-plane) direction. To ensure converged ground state, a rigorous total energy convergence threshold of $7.3 \times 10^{-9} Ry$ was set for self-consistent field (SCF) cycle, whereas a strict force convergence threshold of 3.9×10^{-4} Ry/Bohr was used for the structural relaxation cycle.

Lattice dynamics were investigated via Density Functional Perturbation Theory (DFPT) [40] using the linear response method as implemented in the PHONON package of the Quantum Espresso distribution [37]. Dynamical matrices and the self-consistent first-order variation of the periodic potential (ΔV_{scf}) were computed on a uniform 6×6×1 q-point mesh [40]. The real space interatomic force constants (IFCs) were derived through fourier

interpolation. To accurately capture the quadratic dispersion of the flexural ZA branch, we enforced the acoustic sum rule [41] by accounting for all translational and rotational invariance constraints. This approach ensures the zero-frequency limit at the **Γ** point, resolving the long-range dipole-dipole interactions. Long-range polar corrections were treated using 2D-specific non-analytical term formalism, capturing the q-dependence of LO-TO splitting in the 2D limit [42].

The transport properties in this work are evaluated using the semi-classical Boltzmann Transport Equation (BTE), governing non-equilibrium distribution of charge carriers. The macroscopic transport coefficients are derived from the transport distribution function, $\sigma(\varepsilon, T)$, which integrates the square of the group velocities and the relaxation times over the Brillouin zone [43],

$$\sigma(\varepsilon,T) = \int \sum_b v_{b,\boldsymbol{k}} \otimes v_{b,\boldsymbol{k}}\, \tau_{b,\boldsymbol{k}} \delta\left(\varepsilon - \varepsilon_{b,\boldsymbol{k}}\right) \frac{d\boldsymbol{k}}{8\pi^3} \qquad (2.1)$$

This function is used to calculate the moments of the generalized transport coefficients

$$\mathcal{L}^{\alpha}(\mu,T) = q^2 \int \sigma(\varepsilon,T)(\varepsilon-\mu)^{\alpha}\left(-\frac{\partial f^{(0)}(\varepsilon;\mu,T)}{\partial \varepsilon}\right) d\varepsilon \qquad (2.2)$$

From this integral we obtain the κ_{el}, S and carrier contribution to thermal conductivity as,

$$\sigma = \mathcal{L}^{(0)} \qquad (2.3)$$

$$S = \frac{1}{qT}\frac{\mathcal{L}^{(1)}}{\mathcal{L}^{(0)}} \qquad (2.4)$$

$$\kappa_{el} = \frac{1}{q^2 T}\left[\frac{\left(\mathcal{L}^{(1)}\right)^2}{\mathcal{L}^{(0)}} - \mathcal{L}^{(2)}\right] \qquad (2.5)$$

Now mobility tensor can be calculated by solving BTE, given as [44],

$$\mu_{\alpha\beta} = \frac{g_e e}{\Omega N_{\boldsymbol{k}} n_c} \sum_{n\boldsymbol{k}} v_{n\boldsymbol{k},\alpha} v_{n\boldsymbol{k},\beta} \tau_{n\boldsymbol{k}}^{e-ph} \frac{\partial f_{n\boldsymbol{k}}}{\partial \varepsilon_{n\boldsymbol{k}}} \qquad (2.6)$$

where, Ω denotes volume of the unit cell, N_k is the number of sampling points in the Brillouin zone and g_e, n_c are, respectively, the degeneracy of electrons and the carrier concentration, and $v_{nk,\alpha}$ is the velocity of the single-particle electron with the eigenvalue ε_{nk}. The electron-phonon interaction matrix element $g_{mn\lambda}(k,q)$ is defined as [40],

$$g_{mn\lambda}(\boldsymbol{k},\boldsymbol{q}) = < \psi_{m\boldsymbol{k}+\boldsymbol{q}} | \Delta_{q\lambda} V^{KS} | \psi_{n\boldsymbol{k}} > \qquad (2.7)$$

with ψ_{nk} and ψ_{mk+q} being the initial and final electronic bloch states scattered by the phonon (λ, q), respectively. $\Delta_{q\lambda} V^{KS}$ is the variation of the Kohn-Sham potential induced by

lattice vibrations. The scattering rates of electrons due to EPI can be derived using Fermi's golden rule within the RTA [44]

$$\frac{1}{\tau_{nk}^{e-ph}} = \frac{2\pi}{\hbar}\sum_{m,p}\int \frac{dq}{\Omega_{BZ}} |g_{mn\lambda}(\boldsymbol{k},\boldsymbol{q})|^2 \times [(f_{mk+q} + n_{pq})\delta(\varepsilon_{nk} - \varepsilon_{mk+q} + \hbar\omega_{pq}) + (1 - f_{mk+q} + n_{pq})\delta(\varepsilon_{nk} - \varepsilon_{mk+q} - \hbar\omega_{pq})] \quad (2.8)$$

Here, Ω_{BZ} denote volume of the first Brillouin zone, ε_{nk} represent electron energy of band n at wave vector k, and ω_{pq} is the phonon frequency corresponding to mode p at wave vector q. The terms f_{mk+q} and n_{pq} correspond to the Fermi-Dirac and Bose-Einstein distribution functions, respectively. $g_{mn\lambda}(\boldsymbol{k},\boldsymbol{q}) = \mathrm{M}_{\mathrm{nk,pq}}^{\mathrm{mk+q}}$ represents the electron-phonon matrix elements. The first term on right hand side of equation (1) describes the electron scattering rate associated with phonon absorption, while the second term corresponds to the phonon-emission process.

The implementation of the Wannier interpolation method in the Wannier90 [45] and EPW (electron-phonon Wannier) [46] code generates dense fine grid which describes electron-phonon scattering accurately. To accurately evaluate EPC, we employed coarse 12×12×1 Γ-centred k-point and 6×6×1 Γ-centred q-point grids for the DFPT calculations. To ensure convergence, transport properties were calculated by solving the BTE on dense 80×80×1 k- and q-meshes, obtained via Wannier interpolation of the first-principles results. The real rapid real-space decay of the Wannier tight-binding representations of the Hamiltonian, and electron–phonon matrix elements, and the accurate agreement between the DFT and Wannier interpolated band structures are presented in the Appendix I. We incorporated the analytical long-range correction using framework of Sohier et al. [47] within EPW code. Thermoelectric transport properties were evaluated by solving BTE as implemented in the BoltzTraP2 package [43]. To move beyond the constant relaxation time approximation (CRTA), we explicitly incorporated energy and momentum-dependent scattering rates. State-specific relaxation times were derived from first-principles EPC matrix elements using the EPW code [47]. Long-range Fröhlich only calculations were also implemented in the EPW code. The square-well approximations of the electron density along Z direction [46]:

$$|g^{2D}(q)|^2 = \frac{c}{2\pi}\int_{-\infty}^{\infty} dq_z\, F(q_z)\, |g^{3D}(q,q_z)|^2 \quad (2.9)$$

Where q and q_z are the components of the phonon momentum q parallel and perpendicular to the slab, respectively, c is the slab thickness, and $F(q_z)$ is the Fourier component of the electron density profile along z.

Finally, while the entire transport and scattering workflow relies exclusively on the aforementioned QE framework, the electronic band dispersions and projected Density of States (DOS) presented in this study were independently evaluated using the Vienna Ab initio Simulation Package (VASP) [48-49]. This analysis was performed strictly to determine the atomic orbital contributions to the band edges. The details of the VASP calculation setup, along with a direct comparison demonstrating the excellent agreement between the VASP and QE band dispersions, are provided in the Appendix. The atomic structures of Bi_2X (where **X** = Sn, Ge) were modelled using the VESTA (Visualization for Electronic and Structural Analysis) by applying space-group symmetry to the refined fractional coordinates of the asymmetric unit [50].

2.2 THEORETICAL BASIS

2.2.1 Density Functional Theory

Solving Many-Body Problem: The Schrödinger equation has always been a challenge. For a system of N electrons, wavefunction is a function of 3N dimensions, and it is computationally impossible to solve it. There have been theoretical approaches which considered treating electrons as non-interacting particles but the Coulomb interaction between electrons is a critical component and cannot be neglected. DFT provides a tractable solution to this dilemma. It considers the complex interacting many-electron system as a simple non-interacting electron system that generates an identical ground-state electron density. Its theoretical foundation revolves around the Hohenberg-Kohn Theorem. Instead of using a complex N-electron wave function, DFT uses three-dimensional electron density, $n(\mathbf{r})$. [51]

The first HK theorem states that ground-state electron density of a system determines the unique external potential that generated it and, hence, determines other properties, including the total energy of the system. Its proof lies in the fact that no two different external potentials can generate the same ground-state density. The second theorem, is a variational principle, which states that a universal functional, E[n], exists for energy and that the true

ground state energy of this system is the minimum value of this functional which is achieved only at the true ground state electron density. This theorem proves the existence of this exact energy functional but does not provide its true form. This gap was bridged by the formulation of the Kohn-Sham equations. [51]

Kohn-Sham equations deal with this by replacing the difficult interacting electrons problem with a solvable non-interacting electrons which produce the exact same ground-state density as the real system. It partitions the total energy functional into components that are exactly known and simple to compute and the complex many body quantum mechanics into separate terms. The total energy is broken into three terms: $T_s[n]$, the kinetic energy of non-interacting Kohn-Sham electrons, the electrostatic energy of Coulomb interaction of electron density with itself and with external potential of the nuclei and the exchange-correlation energy $E_{xc}[n]$. This last term is defined to contain everything else including the difference between true kinetic energy and $T_s[n]$ and all non-classical electrostatic contribution. This result in a set of single particle Schrodinger equations which are solved via iterative, self-consistent cycle. First initial electron density is guessed and used to calculate effective potential. KS equations are then solved for this equation for a new set of orbitals of one particle, which gives a new electron density. This process is repeated until we get consistent input and output densities. The accuracy of this process depends on how good approximations are of the exchange-correlation functional. [52]

To find accurate approximations for the exchange-correlation functional, there is a concept of 'Jacob's Ladder' where each rung represents a higher level of sophistication. First comes the LDA, which approximates the exchange-correlation energy at any point in using the exact energy of a uniform electron gas that has the same density as the real system at that point. LDA, because of this simplicity usually lead to bond energies that are too high and bond lengths that are too short. GGA is the next in line which apart from the electron density at a point n(r) also considers the gradient of the density, $\nabla n(r)$. This allows the functional to consider the inhomogeneity of the electron density. This finds much better atomization energies. The PBE functional is a widely used implementation of the GGA, known for its simplicity and construction from fundamental constants. [53]

Mathematical functions known as a basis set are used to solve the orbitals. A plane wave is the most suited basis set for solving a system like a crystal that follows periodicity.

To solve for the core electrons near the nucleus, a vast number of plane waves are required, which is computationally very costly. [54]

This problem is solved using the pseudopotential approximation. Core electrons do not participate in chemical bonding. This approximation removes the core electrons from the calculation and replaces the strong Coulomb potential of the nucleus with a much weaker, smoother effective potential known as the pseudopotential. This makes the valence wavefunctions smooth and in the core region. [54]

2.2.2 Density Functional Perturbation Theory

DFPT extends DFT framework to describes lattice vibrations and the linear electronic response by calculating how electronic ground state changes under small atomic displacements. Within Born-Oppenheimer approximation, ionic motion act as a perturbation to the electronic Hamiltonian, and the resulting forces can be expressed using Hellman-Feynman theorem. The corresponding force relation

$$\frac{\partial E_\lambda}{\partial \lambda_i} = \int n_\lambda(r) \frac{\partial V_\lambda(r)}{\partial \lambda_i} dr \qquad (2.10)$$

forms the basis for calculating harmonic force constants. [55] Instead of relying on explicit atomic displacements, DFPT obtains first-order change in electronic wavefunctions by solving the Sternheimmer-type linear equation

$$(H_{SCF} - \varepsilon_{vk})\Delta\psi_{\{v,k+q\}} = -P_c \Delta V_{SCF} \psi_{\{v,k\}} \qquad (2.11)$$

which eliminates the need for direct summation over conduction bands. This equation connects the perturbing potentials arising from ionic motion with the first order variation of the Kohn-Sham orbitals. [56]

The corresponding change in electronic density is obtained from

$$\Delta n(r) = 4 \sum_{\{v.k\}} \psi^*_{\{v,k\}}(r) \Delta\psi_{\{v,k+q\}}(r) \qquad (2.12)$$

completes the self-consistent linear response cycle. [57]

After calculating responses at selected wave vectors, real-space force constants can be used to interpolate phonon properties across the entire Brillouin Zone using the Fourier relations

$$C_{ij}(R) = \frac{1}{N} \sum_q e^{-iqR} C_{ij}(q), \quad D_{ij}(q) = \sum_R C_{ij}(R) e^{iqR} \qquad (2.13)$$

which provide the connection between real-space and reciprocal space lattice dynamics. This interpolation allows reconstruction of full phonon dispersion without repeating perturbation calculations at each point. [55]

DFPT is known for its computational efficiency, which can be done by reformulating the response in terms of Green's function expression that avoids full diagonalization of the unperturbed Hamiltonian. Therefore, the linear response density is found by

$$\Delta n(q+G) = -\frac{4}{V}\sum_{\{k,v\}}\langle v,k|e^{-i(q+G)r}P_c G_0\big(\varepsilon_v(k)\big)P_c\Delta V_{SCF}|v,k\rangle \quad (2.14)$$

which reduces the scaling of single SCF cycle and removes the need for large supercells. [56]

This allows phonons of any wavelength to be computed independently and efficiently forming the basis of first-principles lattice dynamical calculations. [57]

2.2.3 Wannier Interpolations

Wannier interpolation provides a way to reconstruct electron bands, phonon frequencies, and electron-phonon matrix elements on dense BZ grids using a coarse set of first-principles data. It obtains electronic eigenstates from DFT and vibrational properties from DFPT and transforms them into, first localised Wannier representation and then back to **k** and **q** points through Fourier interpolation. This method reduces the computational cost of electron phonon calculations and as well as retains the first-principles accuracy.

The construction begins by defining electronic Wannier functions from Bloch states through a unitary transformation,

$$|mR_e\rangle = \sum_{nk} e^{-ikR_e}U_{mn,k}|nk\rangle \quad (2.15)$$

With the inverse relation

$$|nk\rangle = \frac{1}{N_e}\sum_{m,R_e} e^{ikR_e}U^{\dagger}_{mn,k}|mR_e\rangle \quad (2.16)$$

which sets up the real space electronic representation

Transforming the Kohn-Sham Hamiltonian then yields

$$H^{el}_{(R_e),R'_e} = \sum_k e^{-ik(R_e-R'_e)}U^{\dagger}_k H^{el}_k U_k \quad (2.17)$$

whose spatial decay causes interpolation of electron energies at arbitrary k points via Fourier reconstruction.

A parallel construction applies to lattice vibration after DFPT. The phonon dynamical matrix is transformed to,

$$D^{ph}_{(R_p),(R'_p)} = \sum_q e^{-iq(R_p - R'_p)} e_q D^{ph}_q e^{\dagger}_q \qquad (2.18)$$

Which connects directly to the interatomic force-constant matrix through

$$\langle \tau_{kp} | \widehat{D}_{ph} | \tau_{k'p'} \rangle = (m_k m_{k'})^{-\frac{1}{2}} C_{kp,k'p'} \qquad (2.19)$$

Establishing the real space formulation for phonon interpolation

The electron phonon interaction in incorporated into the same scheme. Starting from DFPT-computed Bloch-space matrix elements $g_{mn,v}$ (k,q) the joint electron-phonon wannier representation is obtained through

$$g(k,q) = \frac{1}{N_e} \sum_{R_e,R_p} e^{i(kR_e + qR_p)} U_{k+q} g(R_e, R_p) U^{\dagger}_k u_q \quad (2.20)$$

With the localized vertex given by

$$g_{mn,v}(R_e, R_p) = \langle m0_e | \Delta_{(R_p),v} V | nR_e \rangle \qquad (2.21)$$

Because these matrices decay rapidly in both electronic coordinate R_e and the phonon coordinate R_p, only a small set of real space elements is required. Once this compact representation is completed, the full electron-phonon matrix elements can be interpolated to dense k-q meshes, for accurate evaluation of linewidth, Eliashberg functions, and transport coefficients at a low computational cost.

Overall, Wannier interpolation provides a localized and highly effective method that connects coarse first-principles data to dense Brillouin zone sampling. When combined with DFT and DFPT, it forms a complete way for evaluating electron, phonon and electron-phonon properties of materials with first-principles accuracy. [58]

2.2.4 Boltzmann Transport Equation

The study of transport phenomena involves interaction between two opposing mechanisms, the driving force exerted by external fields and the dissipative effects caused by scattering of charge carriers by defects and phonons. These equations serve as the mathematical

framework to describe this phenomenon. It investigates how thermodynamic equilibrium distribution of carriers is modified by external forces and scattering.

Standard fermi distribution f_0 describes the electronic distribution in state of thermal equilibrium. When this equilibrium is disturbed, the relevant distribution function becomes dependent on both position r and time t.

To derive this equation, we consider the evolution of the distribution function f over time interval dt. In a collisionless environment, an electron follows a path defined by group velocity v and field acceleration. But collisions occurring during this interval can scatter electrons into or out of the specific state, which requires a correction term. By expanding this relation linearly with dt, we can obtain the Boltzmann equation:

$$\frac{\partial f}{\partial t} + v\nabla_r f - \frac{e}{\hbar}\varepsilon\nabla_k f = \left(\frac{\partial f}{\partial t}\right)_s \qquad (2.22)$$

The terms on the LHS are known as drift terms and on the right-hand side is the scattering term.

The drift term describes the motion of electron through phase space under smooth external influences.

$\frac{\partial f}{\partial t}$: Represent the time dependence of distribution function

$v\nabla_r f$: Represent the diffusion of carriers due to spatial inhomogeneities.

$-\frac{e}{\hbar}\varepsilon\nabla_k f$: Represent the acceleration of carriers within the Brillouin zone due to the external electric field casuing shift in the wave vector k

Scattering Term accounts for the atomic-scale discontinuous changes in the distribution function due to collisions.

$$\left(\frac{\partial f(k)}{\partial t}\right)_s = \frac{V}{(2\pi)^3}\int dk' \left\{[1-f(k)]w_{k(k')}f(k') - [1-f(k')]w_{(k')k}f(k)\right\} \qquad (2.23)$$

In this integrand first term account for scattering event with transfer of elctrons from occupied states k' to unoccupied state k. The second term accounts for electrons scattered out of the state k to other state k'.

Solving this Boltzmann equation in its general form is complex. Hence, scattering term is frequently modelled using relaxation time. In this model, we consider that the scattering process drives the non-equilibrium distribution f back towards the equilibrium distribution f_0 at a rate proportional to deviations from equilibrium.

$$\left(\frac{\partial f}{\partial t}\right)_s = \frac{-f(k) - f_0(k)}{\tau(k)} \qquad (2.24)$$

Here, τ(k) is relaxation time which depends on the position of the state in k-space. It represents time constant with which the system relaxes exponentially back to the equilibrium state once the external perturbation is removed. [59]

2.3 COMPUTATIONAL PROGRAMS

2.3.1 Quantum Espresso

Quantum Espresso is a collection of open-source tools used to study electronic structure with plane-wave DFT and pseudopotentials. It has different modules which work together to handle tasks such as ground-state calculations, vibrational properties and much more. It is also linked with external utilities like Wannier90 for further analysis and interpolation of electronic properties. [60]

2.3.1.1 EPW

EPW is a quantum espresso module designed to compute electron phonon coupling, transport properties and much more. It works with output of PW and PHonon, and allows fine grid interpolation of electron phonon quantities using Wannier functions. [60]

2.3.1.2 Wannier 90

It is a post-processing code that builds maximally localised Wannier functions starting from Bloch states generated by first-principles calculations. It can transform extended wavefunctions into a compact, real-space from using established localization procedures. When used with PW, it can perform tasks like band interpolation and transport-related studies via pw2wannier90.x [60]

2.3.1.3 PHonon

This performs linear-response calculations for phonon frequencies, eigenvectors and electron-phonon interaction using DFPT. It takes ground-state properties from PW and then generates dynamical matrix at chosen q points. It has tools that can convert these matrices to real-space force constants and produce full phonon dispersions and density of state results. [60]

2.3.1.4 PW

PW is the main plane-wave self-consistent field code in Quantum Espresso. It handles total energies, forces, stress and Kohn-Sham orbitals within DFT. It supports many exchange-correlational functionals and pseudopotential types and can also treat spin orbit effects and much more. It also provides option for structural relaxation, molecular dynamics, polarization calculations etc. [60]

2.3.2 BoltzTrap2

It is a program which generates smooth Fourier-bases interpolations of band energies, and calculates transport coefficients using the linearized BTE. It works on basic input such as energy values on a k-grid and can also include momentum related matrix elements and scattering information. It focuses on giving reliable and automated way to handle periodic electronic data and extract transport coefficients for crystalline systems. [61]

2.3.3 Phonopy

Phonopy is an open-source framework designed to calculate harmonic phonon properties using the supercell approach, built on a consistent description of crystal structure, symmetry and force-constants transformation. It calculates dynamical matrices from these force constants and includes the non-analytical term correction to account for long-range dipole interaction near gamma point. This makes Phonopy reliable for modelling vibrational behaviour in the harmonic approximation. [62]

2.3.4 Phono3py

Phono3py extends phonopy by enabling the calculation of anharmonic properties through three phonon interactions from third force constants. It can manage large sampling requirements using generalised grids, optimized index of q-point triplets and symmetry reduction. Phono3py is reliable for predicting lattice thermal conductivity and other temperature-dependent anharmonic effects. [62]

2.3.5 VESTA

VESTA is a 3D visualization tool for exploring crystal structure and volumetric data in a single interface. We can open several models at once and handle very large structural systems.

It supports geometric analysis, overlays transparent or color-coded iso-surfaces on atomic structures and combine multiple volumetric datasets. It provides smooth rendering and high-resolutions image export and is free for non-commercial use on major platforms. [63]

CHAPTER 3: RESULT AND DISCUSSION

3.1 CRYSTAL STRUCTURE AND PHONON DISPERSION

The relaxed monolayer Bi_2Ge and Bi_2Sn structures crystallize in a penta-type tetragonal lattice belonging to the space group $P\bar{4}2_1m$ (No. 113) [34]. Within this specific symmetry framework, the unit cell comprises six atoms: two group-IV (X = Ge, Sn) atoms occupying the 2b Wyckoff positions and four Bi atoms at the 4e positions [34]. As seen in Fig. 1, the lattice sides connect the 3-coordinated Bi vertices to the 4-coordinated group-IV vertices in a repeating geometric pattern, the structure satisfies the criteria for a special case of mathematical type-4 monohedral tiling, making it structurally and topologically equivalent to the well-known Cairo pentagonal lattice [64]. Therefore, the structure exhibits a vertically buckled geometry. The lattice is inherently non-centrosymmetric, a fundamental characteristic of the $P\bar{4}2_1m$ space group, while the out-of-plane buckling independently reflects the absence of reflection symmetry across the 2D basal plane [34]. These distinct structural asymmetries generate macroscopic electric dipole moments, which permit the inclusion of long-range polar optical and piezoelectric scattering mechanisms alongside short-range interactions [23, 65].

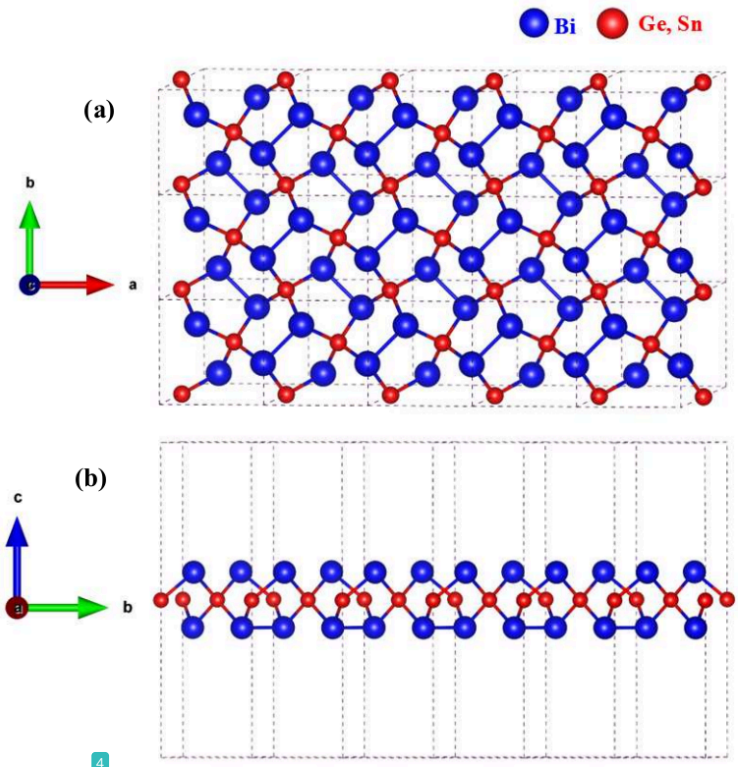

Fig. 1. (a) Top and **(b)** side views of the relaxed crystal structure of monolayer penta-Bi_2X (X = Ge, Sn).

To ensure a highly rigorous baseline for this relaxed geometry, SOC was fully accounted for during the structural relaxation. The calculated structural parameters are summarized in **Table 1.** The in-plane lattice constants for Bi_2Ge and Bi_2Sn are 5.91 Å and 6.24 Å, respectively. These values are in general good agreement with existing literature, the slight difference in lattice parameters is reasonable considering we used fully relativistic ONCV pseudopotentials whereas PAW pseudopotentials were employed in a prior investigation. [34, 38]

Table 1. Optimized structural parameters of relaxed monolayer penta-Bi_2X (X = Ge, Sn).

System	Method	a=b (Å)	Layer Thickness (Å)	Bi-Bi (Å)	Bi-X (Å)
Bi_2Ge	ONCV (This work)	5.91	3.53	3.07	2.79
	PAW [34]	5.85	3.53	3.04	2.77
Bi_2Sn	ONCV (This work)	6.24	3.73	3.06	2.96
	PAW [34]	6.17	3.76	3.03	2.96

Following the structural optimization, the dynamical stability of the penta-Bi_2X (X = Ge, Sn) monolayers was verified through their phonon dispersion curves and PhDOS as depicted in Fig. 2.

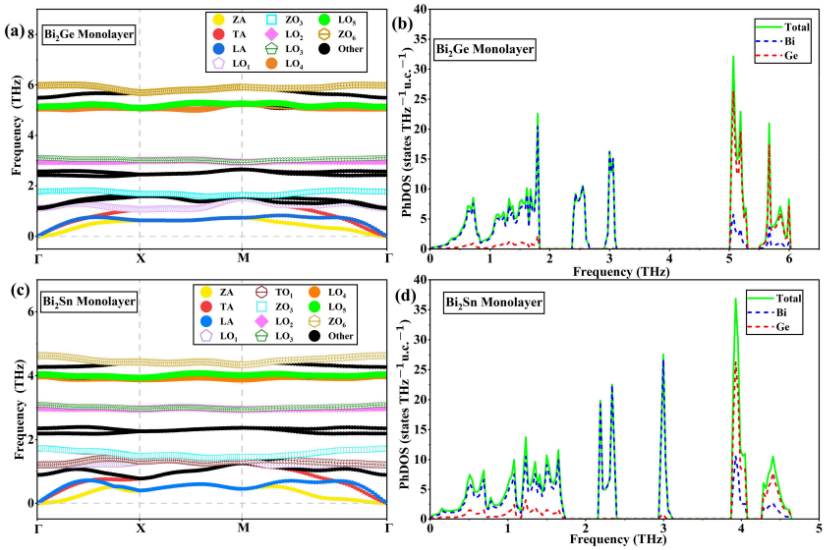

Fig. 2. Calculated phonon dispersion relations along high-symmetry paths and corresponding PhDOS for freestanding monolayer **(a), (b)** Bi_2Ge and **(c), (d)** Bi_2Sn.

The unit cell contains six atoms, resulting in 18 phonon branches. As shown in Fig. 2, the absence of imaginary frequencies throughout Brillouin zone confirms that both monolayers

are dynamically stable. The PhDOS shows a distinct separation based on atomic mass. Due to their significantly larger mass, the heavier Bi atoms dominate the low-frequency acoustic and optical modes spanning up to approximately 3.1 THz for both materials, while the lighter Ge and Sn atoms drive the isolated high-frequency optical spectrum ranging from 5.0 to 6.0 THz for Bi_2Ge, and shifting down to 3.8 to 4.6 THz for Bi_2Sn due to the heavier mass of Sn. Notably, there is no energy gap between the acoustic and the low-lying optical branches. Because the heavy Bismuth atoms predominantly govern the low-frequency regime, the lowest-lying optical branches are dragged down, exhibiting a significant intertwining with the acoustic branches between approximately 1.0 and 1.8 THz for Bi_2Ge and 0.8 to 1.7 THz for Bi_2Sn. This intertwining creates prominent peaks in the PhDOS associated with flat bands. Optical phonon scattering generally reduces at lower temperatures because of statistical occupancy constraints. However, the low energy of these specific optical branches allows them to remain thermally populated and active near room temperature. [45,66]

3.2 ELECTRONIC STRUCTURE

The electronic ground state of the penta-Bi_2X (X = Ge, Sn) monolayers was first elucidated by analysing the band dispersion calculated neglecting SOC [39]. Both monolayers exhibit indirect semiconducting behaviour. For Bi_2Ge, the non-relativistic calculation yields a band gap of 1.120 eV, while Bi_2Sn exhibit a PBE band gap of 1.050 eV. These calculated electronic band structures and band gap values are in good agreement with the prior investigation by Lv et al. [34]. The energy levels at the X and M valleys are nearly degenerate for the VBM while the CBM at the Γ point. For Bi_2Sn, the VBM is located at the M point, while the CBM remains at the Γ point.

Given the large atomic mass of bismuth (Z=83), the SOC interaction is highly significant and leads to a substantial renormalization of the electronic structure [34]. Including SOC significantly narrows the band gaps by approximately 43%, reducing them to 0.632 eV for Bi_2Ge and 0.620 eV for Bi_2Sn, as evident in Fig. 3. (a) and Fig. 3(b). Because the buckled geometry lacks an inversion centre, it creates a potential gradient perpendicular to the atomic layers. This out-of-plane asymmetry interacts with the strong SOC to induce a distinct spin splitting along the high-symmetry paths. This splitting modifies the band edges into a complex camel-back dispersion [67]. Refined grid calculations capture this topology, showing that the true band extrema shift away from the high-symmetry points. In Bi_2Ge, the

VBM and CBM are shifted by 0.106 Å^{-1} and 0.117 Å^{-1} from the **X** and **Γ** points respectively. Similarly, in Bi_2Sn, the VBM shifts 0.057 Å^{-1} away from the **M** valley, while the CBM shifts by 0.141 Å^{-1} from the **Γ** point.

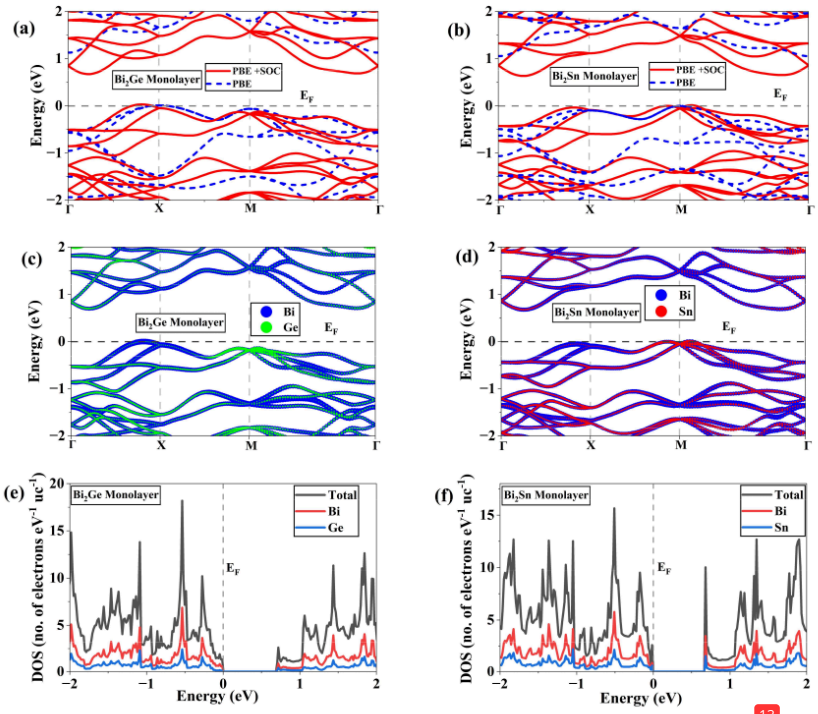

Fig. 3. Electronic properties of monolayer penta-Bi_2X (X = Ge, Sn). The panels display the electronic band structures of monolayer (a) Bi_2Ge and (b) Bi_2Sn calculated using QE (ONCV pseudopotentials) with both PBE and PBE+SOC. Also shown are the atomic-projected band structures of (c) Bi_2Ge and (d) Bi_2Sn, DOS for (e) Bi_2Ge and (f) Bi_2Sn. (c-f) were independently evaluated using VASP (PAW pseudopotentials) to elucidate atomic orbital contributions.

In Fig. 3 (c-f) the atomic-projected band structures and DOS highlight the individual atomic contributions to the overall electronic framework. As discussed by Lv et al., these

electronic states at the band extrema specifically emerge from a profound hybridization between the Bi *p* orbitals and the quasi-sp^3 states of the Ge/Sn atoms. Coupled with the extensive band restructuring driven by SOC, this intrinsic orbital mixing yields notably flattened band edges alongside multiple near-degenerate valleys [34]. To address this band degeneracy, it is necessary to define specific labels for the relevant energy bands. We designate the lowest conduction band as the LCB. For the valence bands, we label them HVB_1 and HVB_2 based solely on their band ordering near the band edges, the uppermost band is defined as the highest valence band (HVB_1), and the band immediately below it is designated as HVB_2. Additionally, when used without further specification in subsequent sections, the abbreviation HVB refers specifically to HVB_1.

As a result of these flattened bands, the DOS rises sharply. While these sharp DOS gradients and multiple carrier valleys provide the necessary electronic foundation for generating a robust *S*, they also increase the available phase space for carrier scattering [7-8, 34] Critically, standard DPT assumes simple parabolic bands and relies heavily on intravalley acoustic scattering at the band edges. The presence of these flat bands and multiple near-degenerate valleys facilitates significant intervalley and interband scattering processes that are overlooked by DPT, thereby underscoring the necessity of a full band and crystal momentum-dependent scattering approach.

3.3 ELECTRON PHONON INTERACTION

3.3.1. Fröhlich Interaction Strength and Decay Characteristics:

The long-range Fröhlich interaction is a major carrier-scattering channel in polar semiconductors. The magnitude of this interaction is governed by the macroscopic electric polarization induced by optical phonons in the long-wavelength limit [23]. Fig. 4 presents the mode-resolved analytical Fröhlich coupling strengths as a function of momentum transfer ($|\mathbf{q}|$) evaluated along the Γ→X direction. These calculations account for both induced polarization effects and the intrinsic dielectric screening of the materials. In Bi_2Ge (Fig. 4a, b), the ZO_3, LO_1, and LO_5 branches are strongly Fröhlich-active and possess large interaction strengths in the small-q regime. Conversely, the LO_2, LO_3, and LO_4 modes remain Fröhlich-silent and display near-zero macroscopic interaction strengths. In Bi_2Sn (Fig. 4c, d), the ZO_3,

LO_1, LO_4, and TO_1 modes dominate the long-range interactions, while the LO_1 mode is remarkably suppressed compared to its Bi_2Ge counterpart.

These mode-specific interaction strengths are fundamentally determined by the coupling between the Born effective charge tensor and the atomic displacement vectors [64]. In Bi_2Ge, the strong couplings of the ZO_3 and LO_1 modes originate from their specific atomic displacement patterns. As a general feature of the long-wavelength limit, the out-of-plane buckling of Bi and Group-IV atoms in the ZO_3 mode generates a substantial in-plane polarization. This polarization is driven by the large off-diagonal elements $(Z^*_{xz}\ and\ Z^*_{yz})$ of the Bi effective charge tensor. Explicit calculations of the induced polarization for small-q phonons approaching along the Γ→X direction are provided in the Supplementary Information to demonstrate how this off-diagonal electromechanical coupling yields a strong Fröhlich interaction.

The in-plane stretching LO_1 mode generates its longitudinal field through a different mechanism involving large in-plane off-diagonal components (Z^*_{xy}). These specific tensor elements prevent the complete cancellation of polarization arising from atomic displacements in different planar directions. The opposing motions of Bi atoms therefore leave a strong net macroscopic dipole when probed along this momentum path. In contrast, the highly symmetric counter-motions in the LO_2, LO_3, and LO_4 branches enforce near-perfect macroscopic dipole cancellation across the unit cell to render them inherently Fröhlich-silent.

The mode-resolved Fröhlich coupling strength (Figure 4) reveals that the LO_1 mode in Bi_2Sn is strongly suppressed due to the destructive interference of the Bi electric dipole moments. This suppression originates from the significantly weaker off-diagonal Born effective charge tensor elements of Bi in Bi_2Sn compared to Bi_2Ge. Specifically, the Z_{xy} and Z_{xz} elements for the Bi atom drop drastically from magnitudes of -0.448 e and -0.541 e in Bi_2Ge, down to just -0.143 e and -0.424 e in Bi_2Sn, respectively (the full 3 × 3 tensor matrices for all atoms are explicitly detailed in Appendix II). Because the LO_1 mode dictates coupled out-of-plane motions within the buckled penta-structure, this severe reduction in both off-diagonal components alters the vector sum of the induced dipoles, leading to the observed destructive interference.

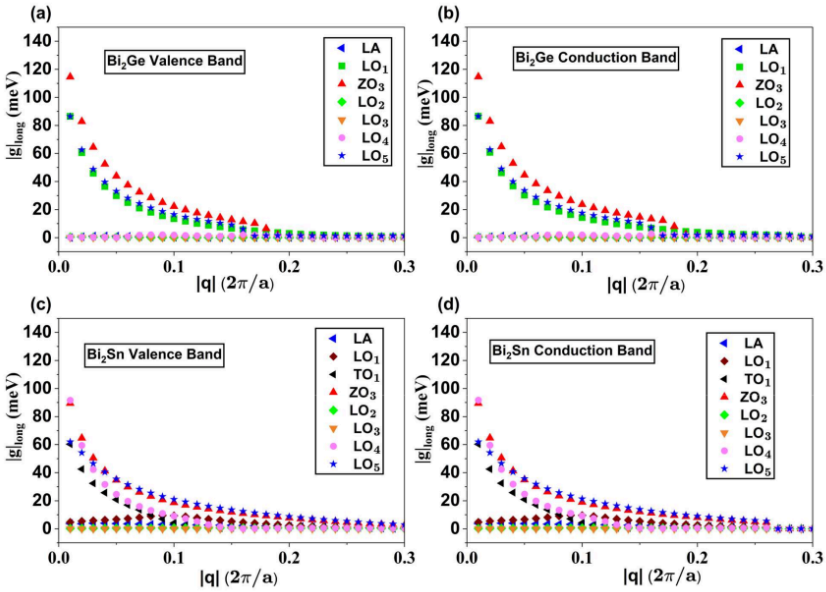

Fig. 4. Mode-resolved long-range Fröhlich coupling strength ($|\boldsymbol{g}|_{\boldsymbol{long}}$) as a function of momentum transfer ($|q|$) evaluated along the Γ→X direction. Results are calculated for a fixed initial state in the VB and CB of (a, b) Bi_2Ge, and **(c**, d) Bi_2Sn.

3.3.2 Electron-Phonon Coupling Strengths for Representative Intra- and Inter-Pocket Transitions

To explore the EPC landscape, a representative set of intra and interpocket transitions were selected for the valence and conduction bands of the Bi_2Ge monolayer and the Bi_2Sn monolayer, as presented in the Fermi surface plots in Fig. 5 and Fig. 7, respectively. The chosen chemical potentials for both materials correspond to an extrinsic carrier concentration of $\sim 1.0 \times 10^{13}\ cm^{-2}$ and are tabulated in Table 2

For Bi_2Ge monolayer transitions $\boldsymbol{q}^{(1)}_{HVB_1 \to HVB_1;\, \Gamma \to X}$, $\boldsymbol{q}^{(1)}_{HVB_2 \to HVB_2;\, \Gamma \to X}$, and $\boldsymbol{q}^{(1)}_{LCB \to LCB;\, \Gamma \to X}$ which involve relatively small crystal momentum transfers of $0.15 \times 2\pi/a$, $0.14 \times 2\pi/a$, and $0.2 \times 2\pi/a$ we observe, as expected, a significant contribution of the Fröhlich part. The $\boldsymbol{q}^{(1)}_{HVB_1 \to HVB_1;\, \Gamma \to X}$ and $\boldsymbol{q}^{(1)}_{HVB_2 \to HVB_2;\, \Gamma \to X}$ represent intrapocket

transitions in the valence band and $\boldsymbol{q}^{(1)}_{LCB\rightarrow LCB;\,\boldsymbol{\Gamma}\rightarrow\boldsymbol{X}}$ is an interpocket from the four-pointed star shape with concave curved sides to the **Γ**pocket in the conduction band. These transitions are particularly chosen towards the tail of the Fröhlich interaction strength singularities that diverge at **Γ** point as shown in Fig. 4, this is a region where an interesting interplay between the Fröhlich interaction and short-range contributions may be expected to be observed. In all of these three transitions involving relatively small crystal momentum transfer in the $\boldsymbol{\Gamma}\rightarrow\boldsymbol{X}$ direction, the strongest electron phonon interaction is found to be mediated by phonons of LO_5, ZO_3, and LO_1 branches. As shown in Fig. 6, while the Fröhlich model calculated coupling strength is close for LO_1 in the HVB_1 transition and also for ZO_3 and LO_5 of LCB, significant differences from the Fröhlich model prediction are observed for this set of $\boldsymbol{\Gamma}\rightarrow\boldsymbol{X}$ intraband nesting vectors in HVB_1, HVB_2 and LCB for certain phonon branches. Most notably, ZO_3 in the two valence-band processes and LO_1 in the conduction-band processes. Thus, it has been illustrated that in addition to the concerns regarding missing the EPI involving large momentum transfer in a Fröhlich only approach, it also seems, that even for transitions in the range where Fröhlich interaction has not decayed, accounting for short-range interactions is important to obtain reliable results.

For the representative processes associated with relatively large crystal momentum transfers, as shown in **Fig. 6** (d-f) for nesting vectors $\boldsymbol{q}^{(3)}_{HVB_1\rightarrow HVB_1;\,\boldsymbol{\Gamma}\rightarrow\boldsymbol{X}}$, $\boldsymbol{q}^{(1)}_{HVB_1\rightarrow HVB_1;\,\boldsymbol{\Gamma}\rightarrow\boldsymbol{M}}$, and $\boldsymbol{q}^{(1)}_{HVB_2\rightarrow HVB_2;\,\boldsymbol{\Gamma}\rightarrow\boldsymbol{M}}$, the Fröhlich interactions become small. However, it is interesting to see that at these larger crystal momentum transfer processes the short-range contributions are nevertheless able to yield EPI strengths in the ~10-20 meV range for many branches. A selection of EPI strengths for branches with the highest EPI strengths is shown in Fig. 6 (d-f). For the $\boldsymbol{q}^{(3)}_{HVB_1\rightarrow HVB_1;\,\boldsymbol{\Gamma}\rightarrow\boldsymbol{X}}$ transition, EPI strengths of ~12 meV, ~10.5 meV and ~ 4.09 meV are observed respectively for ZO_3, LO_5, and ZO_6 processes. It is interesting to note that while the perturbing potential due to this phonon will correspond exactly to that of a phonon with small crystal momentum, the Fröhlich interaction-based perturbing potential does not contribute to a significant interaction strength. We believe that this aspect is due to the different wavefunction profiles of the involved wavefunction, leading to cancellation, as opposed to the $<\psi_f\,|\,\psi_i>\sim 1$ overlap found for the intrapocket transitions with $|\boldsymbol{k}_f-\boldsymbol{k}_i|\sim 0$. For $\boldsymbol{q}^{(1)}_{HVB_1\rightarrow HVB_1;\,\boldsymbol{\Gamma}\rightarrow M}$ nesting vector it is interesting to see the large short-

range part of ~20 meV for the LA branch which is not due to piezoelectric interaction, as is evident from the small $|g_{long}|$ value. This interaction also lies outside the range of applicability of acoustic DPT because for finite q the phonon displacement pattern is, in general, not expressible as a uniform lattice deformation. In transitions due to all three of these nesting vectors, it is also remarkable that ZO_6 branch phonons also mediate a significantly strong interaction, in a purely Fröhlich-based methodology, ZO_6 phonons do not contribute significantly for any $|\boldsymbol{q}|$, and these scattering channels will likely be effectively neglected in such methodologies.

Table 2: Chemical potential corresponding to p- and n-doped Bi_2X (X=Ge, Sn) used for probing EPC strengths

Material	Doping Type	E_F - CBM (eV) (for n-doping)/ E_F - VBM (eV) (for p-doping)
Bi_2Ge Monolayer	p-type (Fig. 5 (a))	-0.13
	n-type (Fig. 5 (b))	0.15
Bi_2Sn Monolayer	p-type (Fig. 7 (a))	-0.07
	n-type (Fig. 7 (b))	0.2

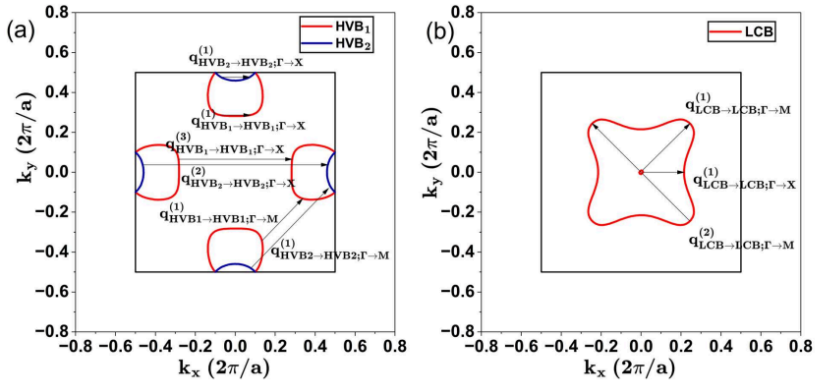

Fig. 5. Fermi surface topology of the Bi_2Ge monolayer. (a) HVB_1 and HVB_2 at μ = VBM - 0.13 eV, (b) LCB at μ = CBM + 0.13 eV

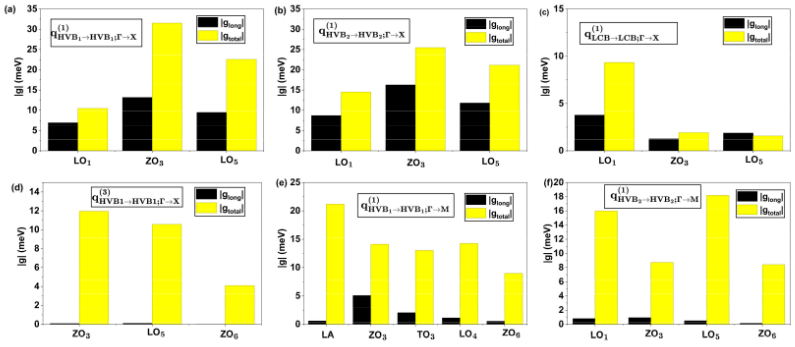

Fig. 6. Penta- Bi_2Ge Monolayer: Comparison of Fröhlich contribution to EPI strength $|g_{long}|$ with total DFPT calculated EPI strength $|g_{total}|$, for representative selection of modes having most dominant EPI strength for nesting vectors: **(a)** $\boldsymbol{q}^{(1)}_{HVB_1\rightarrow HVB_1;\,\Gamma\rightarrow X}$, **(*b*)** $\boldsymbol{q}^{(1)}_{HVB_2\rightarrow HVB_2;\,\Gamma\rightarrow X}$, **(c)** $\boldsymbol{q}^{(1)}_{LCB\rightarrow LCB;\,\Gamma\rightarrow X}$, **(d)** $\boldsymbol{q}^{(3)}_{HVB_1\rightarrow HVB_1;\,\Gamma\rightarrow X}$,**(e)** $\boldsymbol{q}^{(1)}_{HVB_1\rightarrow HVB_1;\,\Gamma\rightarrow M}$, and **(f)** $\boldsymbol{q}^{(1)}_{HVB_2\rightarrow HVB_2;\,\Gamma\rightarrow M}$. **(a-c)** transitions involving small crystal momentum transfer, **(d-f)** transitions involving large crystal momentum transfer

Similarly, for the Bi_2Sn monolayer, representative small $|\mathbf{q}|$ nesting vectors, $\boldsymbol{q}^{(1)}_{HVB_1\rightarrow HVB_1;\,\Gamma\rightarrow X}$, and $\boldsymbol{q}^{(1)}_{HVB_1\rightarrow HVB_1;\,\Gamma\rightarrow M}$ have been chosen with $|\mathbf{q}| \sim 0.1 \times 2\pi/a$. It may be noted that, as compared to the Bi_2Ge monolayer, here the Fröhlich calculated EPI strength and that based on DFPT are close for all Fröhlich active phonon branches. We primarily attribute this to the smaller diameter of the Fermi surface pockets, which decreases the size of typical $|\mathbf{q}|$ for intrapocket transitions, as reflected also by our choice of nesting vectors which have a smaller magnitude than those chosen for the Bi_2Ge monolayer. In the conduction band, we choose for this Fröhlich and short-range part contribution comparison an intermediate vector of $|\mathbf{q}| \sim 0.25 \times 2\pi/a$ which corresponds to an interpocket transition from the four-pointed star shape with concave curved sides to the Γ pocket in the conduction band. Here, except for the LO_5 branch phonon, for all other processes, significant deviation from the Fröhlich model is observed, as expected. For this nesting vector, $\boldsymbol{q}^{(1)}_{LCB\rightarrow LCB;\,\Gamma\rightarrow X}$ a noteworthy EPI strength of ~ 12-18 meV is obtained due to the short range contribution to EPI for LA, ZO_1, and ZO_3 phonons, whereas for the LO_5 branch the short range part is not

able to contribute as significantly, and the total EPI strength is ~5 meV which seems to come primarily from the small Fröhlich interaction for phonons with this large |**q**|. Moving to interpocket transitions involving large crystal momentum transfer, $\boldsymbol{q}^{(1)}_{LCB\rightarrow LCB;\,\Gamma\rightarrow \mathrm{M}}$, $\boldsymbol{q}^{(1)}_{HVB_2\rightarrow HVB_2;\,\Gamma\rightarrow \mathrm{X}}$, and $\boldsymbol{q}^{(2)}_{HVB_1\rightarrow HVB_1;\,\Gamma\rightarrow \mathrm{X}}$ we find a more scattered distribution of epi strengths involving a greater number of important modes as compared to the Bi_2Ge monolayer. Also, interestingly, in contrast with the large momentum transfer processes for the Bi_2Ge monolayer and other transition processes in the Bi_2Sn monolayer, for the $\boldsymbol{q}^{(1)}_{HVB_2\rightarrow HVB_2;\,\Gamma\rightarrow X}$ process, a large contribution due to Fröhlich interaction is found. This is made possible by the fact that the perturbing potential due to this large |q| phonon is indistinguishable from a smaller downfolded |**q**|. However, it is noteworthy to mention that simply having a small |**q**| on downfolding to the first BZ is not sufficient to guarantee a prominent Fröhlich contribution, as seen in the other cases. The coupling strength ~40 meV for the conduction band $\boldsymbol{q}^{(\mathbf{1})}_{\boldsymbol{HVB2\rightarrow HVB2};\,\Gamma\rightarrow \mathrm{X}}$ process contributed by the ZO_6 branch is particularly noteworthy, as is also the coupling strength ~ 23 meV of $\boldsymbol{q}^{(1)}_{HVB_2\rightarrow HVB_2;\,\Gamma\rightarrow \mathrm{X}}$ mediated by ZO_3. Interestingly, the short-range contribution of the EPI allows an EPI of ~20 meV to be maintained, which is close to the Fröhlich dominated magnitude found for the $q^{(1)}_{HVB_1\rightarrow HVB_1;\,\Gamma\rightarrow X}$ nesting vector with $|\mathbf{q}| \sim 0.1\times 2\pi/a$.

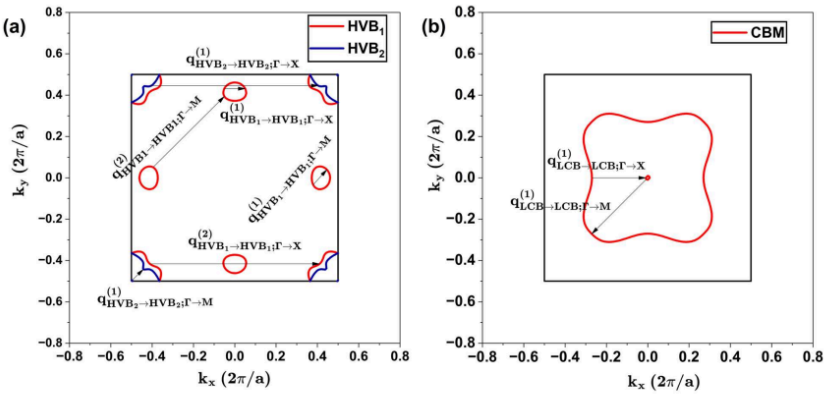

Fig. 7. Fermi surface plots for Bi_2Sn monolayer **(a)** HVB_1 and HVB_2 at μ = VBM - 0.07 eV, and **(b)** LCB at μ = CBM + 0.20 eV

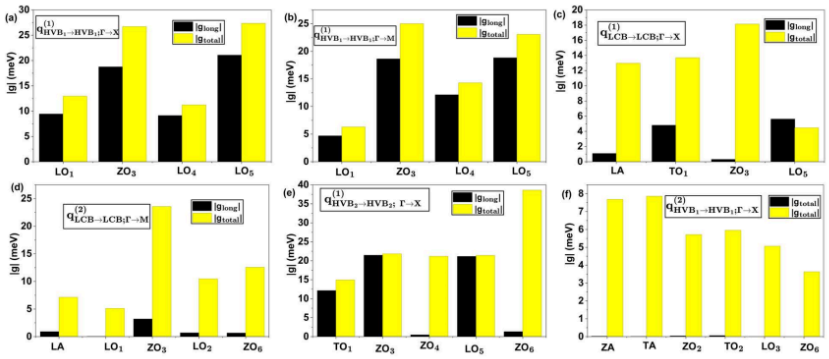

Fig. 8. Penta- Bi_2Sn Monolayer: Comparison of Fröhlich contribution to EPI strength $|g_{long}|$ with total DFPT calculated EPI strength $|g_{total}|$, for representative selection of modes having most dominant EPI strength for nesting vectors:(a) $\boldsymbol{q}^{(1)}_{HVB_1\rightarrow HVB_1;\,\Gamma\rightarrow X}$, (b) $\boldsymbol{q}^{(1)}_{HVB_1\rightarrow HVB_1;\,\Gamma\rightarrow M}$, (c) $\boldsymbol{q}^{(1)}_{LCB\rightarrow LCB;\,\Gamma\rightarrow X}$, **(d)** $\boldsymbol{q}^{(2)}_{LCB\rightarrow LCB;\,\Gamma\rightarrow M}$,**(e)** $\boldsymbol{q}^{(1)}_{HVB_2\rightarrow HVB_2;\,\Gamma\rightarrow X}$, and **(f)** $\boldsymbol{q}^{(2)}_{HVB_1\rightarrow HVB_1;\,\Gamma\rightarrow X}$. (a-b) transitions involving small crystal momentum transfer, (c) transition with intermediate magnitude momentum transfer, and (d-f) transitions involving large crystal momentum transfer

3.3.3 Mode-Resolved Scattering Rates Beyond the Dielectric Continuum Approximation:

To shed light on the extent of applicability of the Fröhlich model for present materials, we compare the mode-resolved scattering rates from the DFPT + Wannier approach to those derived from purely analytical expressions for 2D materials, following Brunin et al. [43]. For both types of calculations, the implementation in EPW is used. Several interesting features are noted. Fig. 9 and Fig. 10 compare these scattering rates for HVB and LCB, respectively. For both of the present materials, the HVB, band edge occurs close to the X point, and additionally, a near valley degeneracy occurs close to the M point of the Brillouin Zone, about ~0.15 eV below the X band edge. Due to thermal smearing, the M point is also expected to be significantly populated even at the lowest levels of doping considered. Moreover, for much of the doping range considered $(n_h > 4 \times 10^{11} cm^{-2})$, the chemical potential already lies below the M band edge. At the M-valley in Bi_2Ge, the DFPT-computed total scattering rate (~1.10×10^{15} s^{-1}) exceeds the Fröhlich prediction (~2.55×10^{14} s^{-1}) by a factor of 4.3. A similar significant deviation occurs in Bi_2Sn at the X-valley, where total scattering is 4.02 times the polar baseline. Finite-momentum intervalley transitions and short-range intravalley mechanisms constitute 64% to 77% of the overall carrier relaxation rate in the HVB.

Evaluating the specific phonon processes mediating HVB carrier relaxation near the band edges reveals that the ZO_6, LO_1, and ZO_3 branches provide the most significant scattering contributions. The highest-frequency ZO_6 branch is particularly noteworthy because the macroscopic Fröhlich model fails to capture the significant electron-phonon coupling (EPC) it induces in the valence band states. Analysing the explicit phonon eigenvectors reveals the microscopic origin of this coupling and its pronounced momentum (q) dependence. For large |q| transitions, particularly those close to the Brillouin zone boundaries that dictate the high scattering rates of zone-edge electronic states, the ZO_6 mode manifests as an out-of-plane optical vibration featuring z-axis buckling. In this region, the two group-IV atoms (Ge/Sn at the 2b Wyckoff positions) in the unit cell oscillate out-of-phase, with a phase angle between $\pi/2$ and π. We propose that the resulting substantial variations in the local Bi–Ge/Sn–Bi bond angles drive the short-range deformation potential responsible for the high scattering rates of the highest valence band (HVB) states. In contrast, the small |q| limit features nearly in-phase

Ge/Sn vibrations, which remain Fröhlich-inactive due to a vanishing mode Born effective charge.

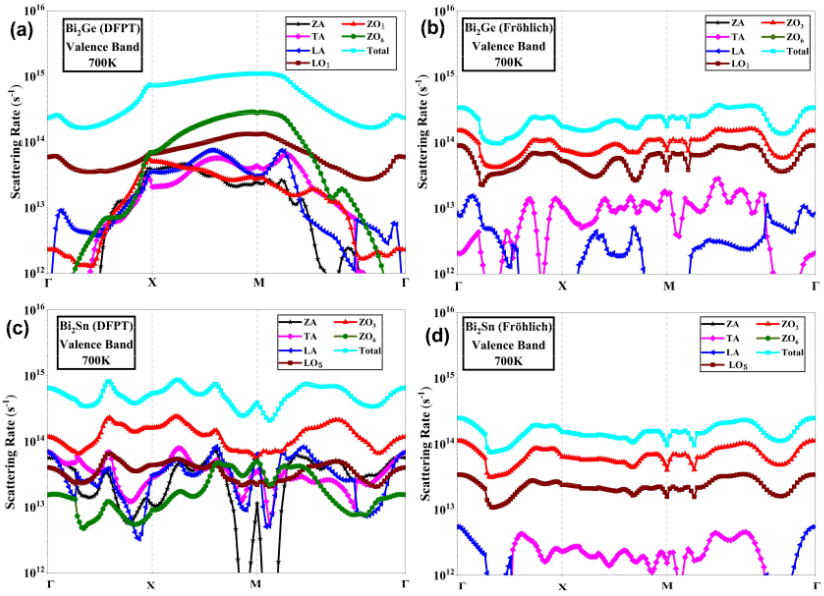

Fig. 9. Mode-resolved electron-phonon Scattering rates for HVB states along high-symmetry paths for **(a)** Bi_2Ge full DFPT, **(b)** Bi_2Ge Fröhlich, **(c)** Bi_2Sn full DFPT, **(d)** Bi_2Sn Fröhlich

For n-type transport in the lowest conduction band (LCB), the two materials exhibit divergent electron-phonon coupling behavior. In the Bi_2Ge LCB, the total scattering rate is suppressed to approximately 47% of the Fröhlich baseline. This reduction originates from destructive interference between macroscopic long-range polar fields and microscopic short-range deformation potentials, predominantly within the ZO_3 and LO_1 optical modes. Conversely, LCB transport in Bi_2Sn is characterized by constructive short-range scattering, where the LA mode exhibits a nearly twelve-fold increase in scattering strength relative to the Fröhlich estimate.

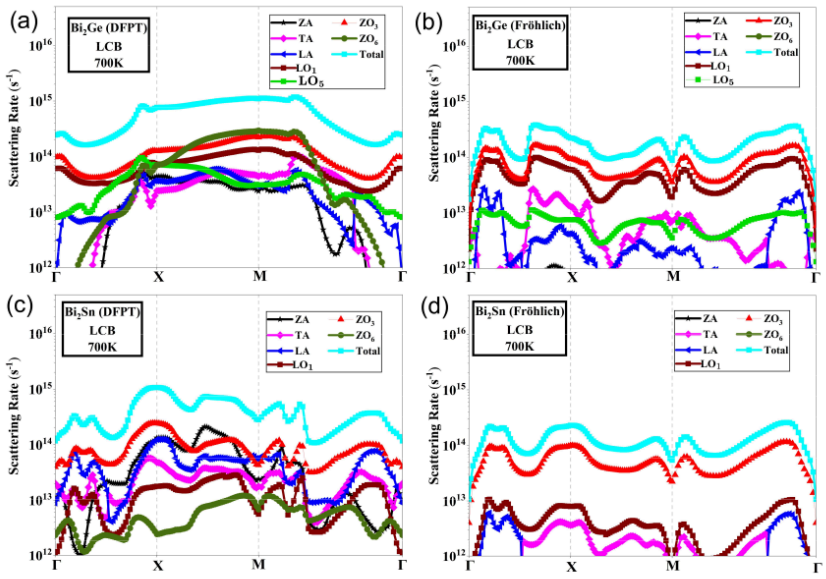

Fig. 10. Mode-resolved electron-phonon Scattering rates for LCB states along high-symmetry paths for the dominant acoustic and optical phonon branches for **(a)** Bi_2Ge full DFPT, **(b)** Bi_2Ge Fröhlich, (c) Bi_2Sn full DFPT, **(d)** Bi_2Sn Fröhlich

3.4 ENERGY-DEPENDENT CARRIER RELAXATION DYNAMICS

To determine the ultimate impact of EPI matrix elements on carrier mobility, the state-specific carrier relaxation times (τ_{nk}) (from eq. (2.8)) for both monolayers were evaluated across the Brillouin zone using the EPW framework [47]. **Fig. 11** shows the energy-dependent lifetimes for both penta-Bi_2Ge and penta-Bi_2Sn monolayers at temperatures of 300K, 550K, and 700K. These lifetimes remain quite short restricted to low-femtosecond regime, 1 to 12 fs for Bi_2Ge and 1 to 16 fs for Bi_2Sn, even at the very edges of the band extrema.

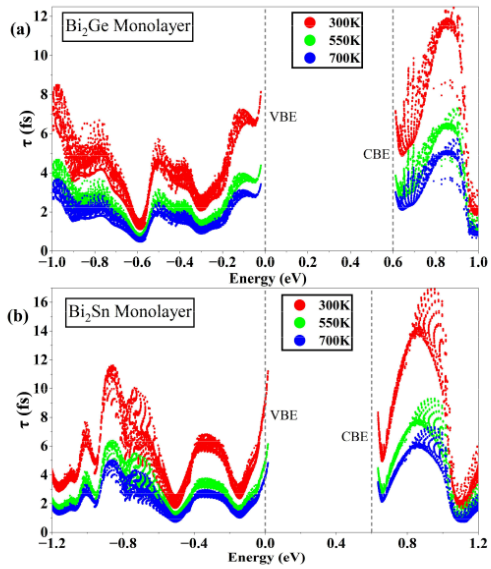

Fig. 11. Calculated τ as a function of energy for monolayer **(a)** penta-Bi_2Ge and **(b)** Bi_2Sn at 300 K, 550 K, and 700 K.

A comparative analysis of the data in Fig. 11. reveals the subtle differences in carrier lifetimes between the two monolayers, with Bi_2Sn maintaining slightly longer lifetimes (by ~3-4 fs) in certain energy regimes. Both materials exhibit highly restricted lifetimes because their scattering landscapes are dominated by short-range intervalley and interband processes. As seen in Section 3.3.3, these short-range mechanisms constitute up to 77% of the total relaxation rate. The anomalous suppression of the long-range LO_1 Fröhlich interaction (as seen in 3.3.1) plays only a secondary role in its transport dynamics.

Furthermore, the vertical spread of data points in **Fig. 11** is a consequence of the complex multi-valley band topology and the resulting state-specific scattering phase space. As established in Section 3.3.3, these materials possess multiple valleys separated by finite energy offsets (e.g., the **M**-valley residing ~0.15 eV below the **X**-valley band edge in the HVB). Because the onset of optical phonon emission requires carriers to possess a minimum kinetic energy equal to the phonon energy, carriers residing at the exact same absolute energy level but in different valleys face a drastic imbalance between absorption and emission

processes. A carrier deep within one valley may have enough kinetic energy to emit optical phonons (resulting in rapid scattering), while a carrier at the exact same energy but near the edge of an offset valley can only absorb phonons. Coupled with the inherent momentum-space anisotropy of the electron-phonon matrix elements, this state-specific availability of emission channels causes carriers at the same energy level to exhibit significantly different relaxation times depending on their specific wavevector. By explicitly calculating these state-specific total transition rates, which isotropic approximations inherently collapse into a single average line, we provide a critical refinement to previous acoustic-only models and capture the full complexity of the scattering landscape in these monolayers.

3.5 MACROSCOPIC THERMOELECTRIC TRANSPORT PROPERTIES AND FIGURE OF MERIT

The calculated macroscopic transport coefficients for penta-Bi_2X (X = Ge, Sn) monolayers demonstrate the critical impact of accounting for full EPI. As expected, in p-type Bi_2Ge at 700 K S peak at 410.99 μVK^{-1} decreases to a lower value of 58.39 μVK^{-1} (Fig. 12, (a)) with increasing carrier concentration from ~10^{11} to ~10^{13} cm^{-2}, because the E_F shifts deeper into the bands, which reduces the weighted energy difference in the transport distribution function, as defined by eq. (4). The n- and p-type Bi_2Sn shows consistent results at 700K and 10^{13} cm^{-2} when comparing the DPT baseline to the EPI framework. In concentration range 10^{12} to 10^{14} cm^{-2} the magnitude of S decreases almost linearly as expected from temperature 300K to 700K. Similar trend in S is also seen for n-type Bi_2Sn (Fig. S4.10 (a) in supplementary information (SI)). While phosphorene offers a high room-temperature S of 510 μVK^{-1} [19], the unique combination of heavy atom induced anharmonicity and band degeneracy in pentagonal Bi_2Sn type framework provides a more robust high-temperature TE response (Fig. 13, (a)).

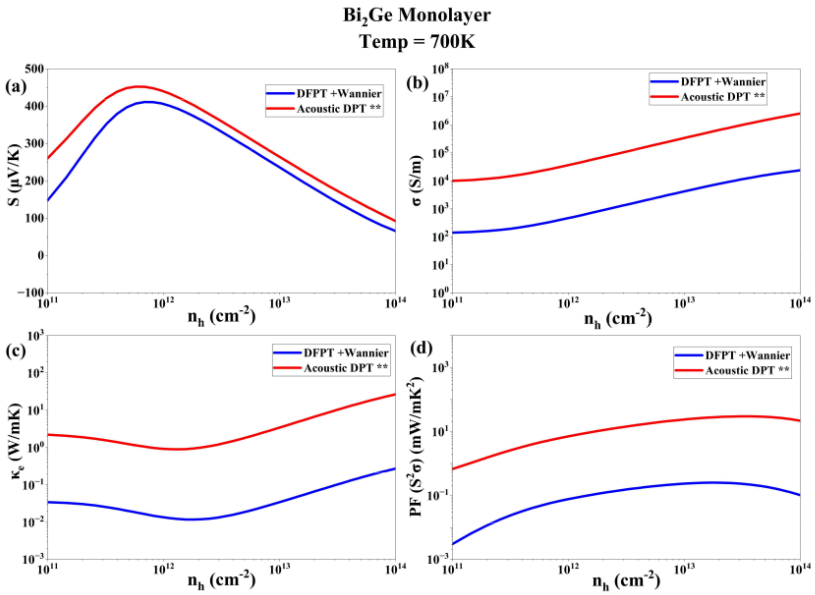

Fig. 12. Thermoelectric transport coefficients of p-type Bi_2Ge plotted against extrinsic hole concentration (n_h) at 700K: **(a)** S, **(b)** σ, **(c)** κ_e, and **(d)** PF = $S^2\sigma$. ** The carrier relaxation time for Acoustic DPT calculation were taken from Lv et al [34]

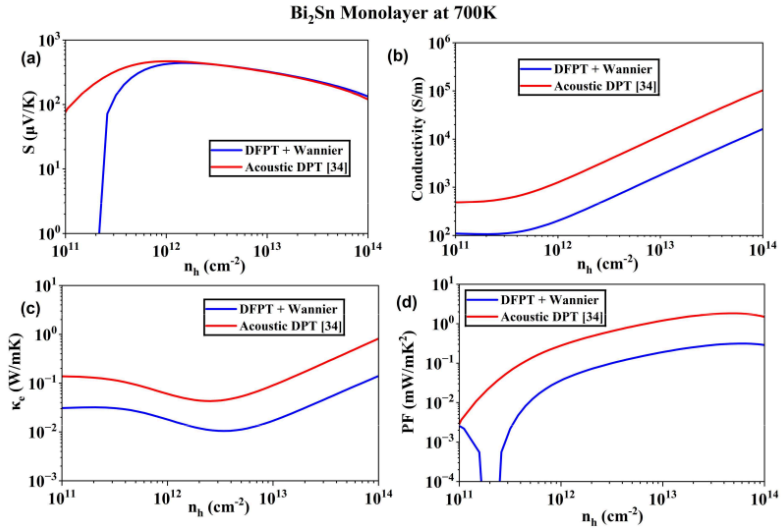

Fig. 13. Thermoelectric transport coefficients of n-type Bi_2Sn plotted against extrinsic hole concentration $(\boldsymbol{n_h})$ at 700K: **(a)** S, **(b)** σ, **(c)** κ_e, and **(d)** PF = $S^2\sigma$. ** The carrier relaxation time for Acoustic DPT calculation were taken from Lv et al [34]

Furthermore, the σ and κ_{el} increases with carrier concentration for both materials as can be seen in Fig. 12, 13 (b), (c). The σ ranges from $1.35 \times 10^2\ Sm^{-1}$ to $2.27 \times 10^4\ Sm^{-1}$ for p-type Bi_2Ge and from $120.74\ Sm^{-1}$ to $3.87 \times 10^4\ Sm^{-1}$ for p-type Bi_2Sn. This is because σ is directly proportional to the transport distribution function as in eq. 3, while κ_{el} is derived from the generalized transport moments in eq. 5. The PF as a function of $\boldsymbol{n_h}$ is represented in Fig. 12, 13(d). It can be seen that PF increases at initial concentrations from 10^{11} to 10^{13} cm^{-2} and then have a slight downfall at 10^{14} cm^{-2}. At 700 K and a carrier concentration of 10^{12} cm^{-2}, the PF value at peak ZT in the p-type Bi_2Ge and p-type Bi_2Sn and undergoes high correction from approximately 13.72 $mWm^{-1}K^{-2}$ to 0.24 $mWm^{-1}K^{-2}$ (Fig. 12(d)) and from 1.24 $mWm^{-1}K^{-2}$ to 0.215 $mWm^{-1}K^{-2}$ (Fig. 13(d)) respectively. This shift is fundamentally driven by the balance between transport coefficient; as doping increases, the decay of S^2 in the PF must be offset by a sufficient rise in σ. Because in our mode-resolved

analysis (Fig. 10), the explicit inclusion of short-range optical and intervalley scattering restricts carrier lifetimes to the low-femtosecond regime, a higher carrier concentration is required to achieve the necessary σ for peak performance. While DPT model predicted high ZT at light doping levels such as $4.16 \times 10^{11} cm^{-2}$ for p-type Bi_2Ge and $1.67 \times 10^{11} cm^{-2}$ for p-type Bi_2Sn, our results show that peaks occur at much higher concentrations of the order of 10^{13} cm^{-2}. This prevents the unphysical high-temperature (at 700K) divergence of κ_{el} as seen in Fig. 12(c), 13(c).

To evaluate the intrinsic thermoelectric performance of penta-Bi_2X (X = Ge, Sn) monolayers, we first compare our findings with the theoretical upper bounds established by Lv et al. using the acoustic deformation potential (DP) approximation. While the DP model provides a valuable initial assessment by projecting peak ZT values of 6.96 for Bi_2Ge and 5.79 for Bi_2Sn at 700 K [34], incorporating comprehensive electron-phonon Wannier scattering refines the peak ZT of p-type Bi_2Ge to approximately 1.00. Bi_2Sn, however, demonstrates notable resilience to these scattering mechanisms, maintaining high peak value of 4.44 (p-type) at its optimal operating temperature of 700 K. Comparing these materials at their specific optimal temperatures suggests that the theoretical high-temperature performance of penta-Bi_2Sn is highly competitive within the broader 2D pentagonal family. For instance, penta-silicene reaches its peak ZT of 3.43 (hole-doped) and 3.04 (electron-doped) at 300 K, whereas penta-GeC_5 achieves a maximum ZT of 6.26 at 900 K [31-32].

While the total ZT of 4.4 for p-type Bi_2Sn remains highly competitive despite the severe degradation of electrical conductivity, it is crucial to recognize the physical origin of this resilience. This relative robustness is mathematically contingent upon the notably low lattice thermal conductivity ($\kappa_l \sim 10^{-2}$ W m^{-1} K^{-1}) inherited from prior theoretical predictions [34]. While the 6.5 Å interaction cutoff employed for third-order force constants in those previous studies is not intrinsically unreasonable, it sits at the lower end of typical interaction limits. Given the extreme 10^{-2} W m^{-1} K^{-1} result it yielded, this baseline warrants intense future scrutiny via fully converged ab initio evaluations to ensure longer-range anharmonic interactions are not prematurely truncated. Nevertheless, adopting this baseline allows the concurrent order-of-magnitude drop in the κ_e to partially compensate for the reduced electrical conductivity. If future ab initio phonon transport evaluations reveal a more conventional, higher κ_l for these crystalline networks, the compensatory leverage provided

by the κ_e reduction would be negated, leading to a profound collapse of the final figure of merit.

CHAPTER 4 : CONCLUSIONS

4.1 CONCULSIONS

In this work, the thermoelectric transport properties of penta-Bi_2X (X = Ge, Sn) monolayers have been systematically investigated using a first-principles EPI framework, considering all scattering processes. Our results underscore that traditional acoustic DPT-based models can substantially overestimate predicted performance in non-centrosymmetric materials with non-vanishing Born effective charge tensors or multiple band and valley degeneracies in electronic structure. We find that the intrinsic mobility in both materials is predominantly restricted by specific high-frequency optical branches, notably due to Fröhlich interactions arising from long-wavelength out-of-plane modes involving anti-phase Bi vertical oscillations. Furthermore, we identify a distinct high-frequency optical mode as a critical driver of intervalley scattering. This mode involves a high-amplitude, out-of-phase vertical oscillation of the Bi atoms against a nearly stationary group-IV framework. Crucially, due to cancellation effects in the Born effective charge tensor, this symmetric out-of-plane displacement renders the mode Fröhlich-inactive. Yet, it still establishes a dominant transport bottleneck that restricts carrier lifetimes to the low-femtosecond regime. While both materials undergo substantial scattering-induced degradation compared to earlier DPT estimates, Bi_2Sn emerges as the superior candidate. Specifically, the predicted PF at optimal performance for p-type Bi_2Ge at 700 K undergoes a drastic downward correction from approximately 13.72 $mWm^{-1}K^{-2}$ to 0.24 $mWm^{-1}K^{-2}$, which is comparatively substantial for p-type Bi_2Sn from 1.24 $mWm^{-1}K^{-2}$ to a corrected PF of 0.215 $mWm^{-1}K^{-2}$ at 700 K. The ionized impurity scattering at high carrier concentrations may further modulate these values, our analysis demonstrates that the fundamental transport trends and the relative superiority of Bi_2Sn remain robust. Ultimately, this study illustrates that for non-centrosymmetric penta-materials featuring polar bonds and multiple valley degeneracies, relying solely on acoustic

deformation potential theory is insufficient. It is fundamentally essential to incorporate the effects of long-range Fröhlich and large-momentum intervalley scattering to achieve a qualitatively accurate and physically rigorous understanding of charge-carrier transport in 2D penta-materials.

APPENDIX I

Validation of Maximally Localized Wannier Functions

To elucidate the reliability of the electron-phonon calculations, we verified the quality of the Wannier model. The figures below demonstrate the exact agreement between the standard DFT and Wannier-interpolated band structures, alongside, the rapid spatial decay of the matrix elements.

A I.1 ACCURACY OF ELECTRONIC BAND INTERPOLATION

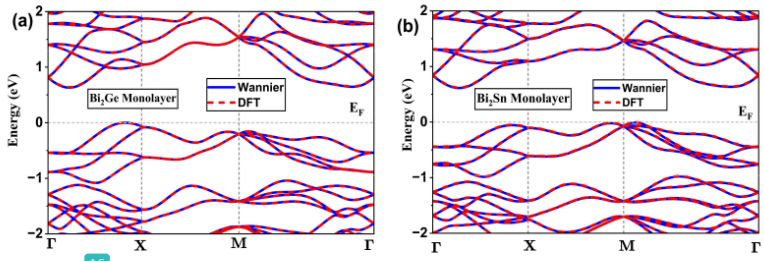

Fig. A I.1: Electronic band structure of (a) Bi_2Ge monolayer and (b) Bi_2Sn monolayer. The exact overlap between the standard DFT calculation and the Wannier interpolation confirms the accuracy of the electronic model.

A I.2: REAL-SPACE DECAY OF MATRIX ELEMENTS

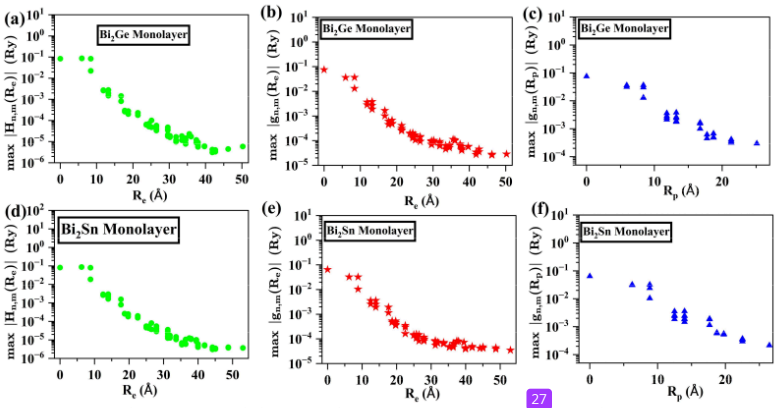

Fig. A I.2: Real-space spatial decay of the maximum Wannier matrix elements for Bi_2Ge (a–c) and Bi_2Sn (d–f). The plots show the exponential drop-off of the Hamiltonian, and the electron phonon band as a function of distance, confirming that the Wannier orbitals are properly localized.

APPENDIX II

Dielectric and Born Effective Charge Tensors

The macroscopic high-frequency dielectric permittivity (ϵ^{∞}) and Born effective charge (Z^{*}) tensors for the penta-Bi_2X (X = Ge, Sn) monolayers were rigorously computed using Density Functional Perturbation Theory (DFPT) within the linear response framework. These calculations were executed using the PHONON package of the Quantum ESPRESSO distribution.

A II.1 HIGH-FREQUENCY DIELECTRIC TENSORS

The computed macroscopic high-frequency dielectric tensors (ϵ^{∞}) for the Bi_2Ge and Bi_2Sn monolayers, evaluated in Cartesian coordinates (x,y,z), are presented below. Due to the two-dimensional nature of the simulated models, which incorporate a 20 Å vacuum gap along the out-of-plane axis, the out-of-plane dielectric component (ϵ^{∞}_{zz}) naturally approaches the vacuum limit (≈1.000).

(a) Penta-Bi_2Ge Monolayer

$$\epsilon^{\infty}(Bi_2Ge) = \begin{bmatrix} 6.407 & 0.000 & 0.000 \\ 0.000 & 6.407 & 0.000 \\ 0.000 & 0.000 & 1.457 \end{bmatrix}$$

(b) Penta-Bi_2Sn Monolayer

$$\epsilon^{\infty}(Bi_2Sn) = \begin{bmatrix} 6.409 & 0.000 & 0.000 \\ 0.000 & 6.409 & 0.000 \\ 0.000 & 0.000 & 1.462 \end{bmatrix}$$

A II.2 BORN EFFECTIVE CHARGE TENSORS

The Born effective charge tensors (Z^{*}), computed in Cartesian coordinates (x,y,z) and presented in units of elementary charge (e), are given below for the individual atoms in the

unit cell. The Acoustic Sum Rule (ASR) has been rigorously applied to ensure exact charge neutrality.

(a) Penta-Bi_2Ge Monolayer

$$Z^*(\text{Bi (1)}) = \begin{bmatrix} -0.524 & -0.448 & -0.541 \\ -0.448 & -0.524 & -0.541 \\ 0.020 & 0.020 & -0.001 \end{bmatrix}, \quad Z^*(\text{Bi (2)}) = \begin{bmatrix} -0.524 & 0.448 & 0.541 \\ 0.448 & -0.524 & -0.541 \\ -0.020 & 0.020 & -0.001 \end{bmatrix}$$

$$Z^*(\text{Bi (3)}) = \begin{bmatrix} -0.524 & -0.448 & 0.541 \\ -0.448 & -0.524 & 0.541 \\ -0.020 & -0.020 & -0.001 \end{bmatrix}, \quad Z^*(\text{Bi (4)}) = \begin{bmatrix} -0.524 & 0.448 & -0.541 \\ 0.448 & -0.524 & 0.541 \\ 0.020 & -0.020 & -0.001 \end{bmatrix}$$

$$Z^*(\text{Ge (1)}) = \begin{bmatrix} 1.049 & 0.528 & 0.000 \\ -0.528 & 1.049 & 0.000 \\ 0.000 & 0.000 & 0.002 \end{bmatrix}, \quad Z^*(\text{Ge (2)}) = \begin{bmatrix} 1.049 & -0.528 & 0.000 \\ 0.528 & 1.049 & 0.000 \\ 0.000 & 0.000 & 0.002 \end{bmatrix}$$

(b) Penta-Bi_2Sn Monolayer

$$Z^*(\text{Bi (1)}) = \begin{bmatrix} -0.798 & -0.143 & -0.424 \\ -0.143 & -0.798 & -0.424 \\ 0.020 & 0.020 & -0.018 \end{bmatrix}, \quad Z^*(\text{Bi (2)}) = \begin{bmatrix} -0.798 & 0.143 & 0.424 \\ 0.143 & -0.798 & -0.424 \\ -0.020 & 0.020 & -0.018 \end{bmatrix}$$

$$Z^*(\text{Bi (3)}) = \begin{bmatrix} -0.798 & -0.143 & 0.424 \\ -0.143 & -0.798 & 0.424 \\ -0.020 & -0.020 & -0.018 \end{bmatrix}, \quad Z^*(\text{Bi (4)}) = \begin{bmatrix} -0.798 & 0.143 & -0.424 \\ 0.143 & -0.798 & 0.424 \\ 0.020 & -0.020 & -0.018 \end{bmatrix}$$

$$Z^*(\text{Sn (1)}) = \begin{bmatrix} 1.597 & 0.500 & 0.000 \\ -0.500 & 1.597 & 0.000 \\ 0.000 & 0.000 & 0.036 \end{bmatrix}, \quad Z^*(\text{Sn (2)}) = \begin{bmatrix} 1.597 & -0.500 & 0.000 \\ 0.500 & 1.597 & 0.000 \\ 0.000 & 0.000 & 0.036 \end{bmatrix}$$

APPENDIX III

Atomic Displacements of Key Fröhlich-Active and Silent Modes

To elucidate the physical origin of the macroscopic electric polarizations discussed in the main text, the atomic displacement patterns for the key optical phonon modes in the long-wavelength limit (q→0) are presented below. These eigenvectors correspond to the LO/TO split limits evaluated specifically as the momentum vector approaches the Γ point along the Γ→X direction.

A III.1

I. Penta-Bi_2Ge Monolayer

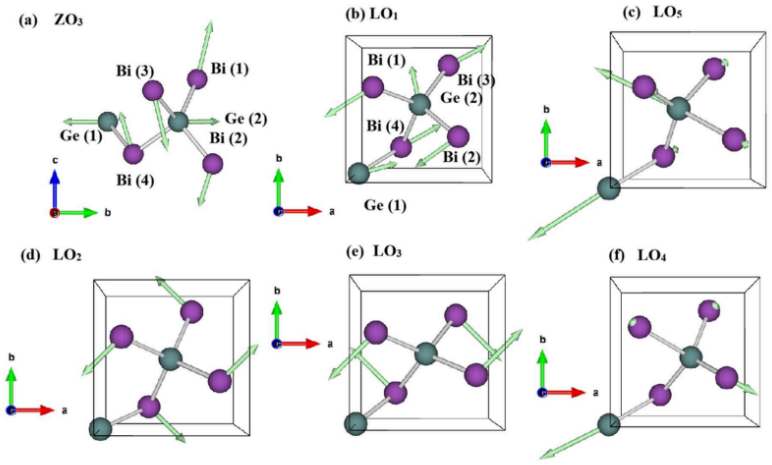

Fig A III.1: Schematic representation of the atomic displacements for key optical phonon modes in the penta-Bi_2Ge monolayer at the Γ point. The highly Fröhlich-active modes include the (a) ZO_3 out-of-plane buckling mode, (b) LO_1 in-plane stretching mode, and (c) LO_5 mode. The inherently Fröhlich-silent modes, characterized by symmetric counter-motions, include the (d) LO_2, (e) LO_3, and (f) LO_4 branches.

II. Penta-Bi_2Sn Monolayer

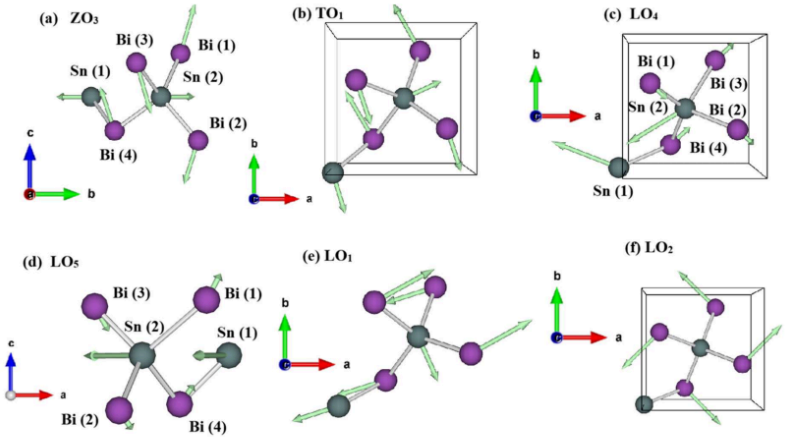

Figure A III.2: Schematic representation of the atomic displacements for key optical phonon modes in the penta-Bi_2Sn monolayer at the Γ point. The dominant Fröhlich-active modes in this system include the (a) ZO_3 and (b) ZO_1 out-of-plane buckling modes, alongside the (c) LO_4 and (d) LO_5 branches. Panel (e) depicts the LO_1 in-plane stretching mode; although it exhibits lateral displacements analogous to its Bi_2Ge counterpart, it is anomalously Fröhlich-suppressed in Bi_2Sn due to weaker off-diagonal effective charge tensor elements and subsequent destructive interference. Panel (f) illustrates the inherently Fröhlich-silent LO_2 mode, driven by highly symmetric counter-motions that enforce macroscopic dipole cancellation.

A III.2 PHONON EIGENVECTORS

The corresponding normalized displacement vectors (u), expressed in Cartesian coordinates (x,y,z), are tabulated below. For all mode eigenvectors, the six rows correspond

to the displacements of atoms Bi(1), Bi(2), Bi(3), Bi(4), X(1), and X(2) (where X = Ge or Sn), respectively.

I. Penta-Bi_2Ge Monolayer

$$\boldsymbol{u}(ZO_3) = \begin{bmatrix} -0.030 + 0.011i & -0.119 - 0.011i & -0.474 - 0.005i \\ -0.002 + 0.007i & 0.113 + 0.017i & 0.337 + 0.027i \\ -0.033 - 0.013i & -0.113 + 0.003i & 0.472 + 0.033i \\ -0.005 - 0.008i & 0.108 - 0.008i & -0.337 + 0.000i \\ 0.043 - 0.001i & 0.361 - 0.009i & 0.002 + 0.002i \\ 0.163 + 0.006i & -0.331 - 0.013i & -0.004 + 0.000i \end{bmatrix}$$

$$\boldsymbol{u}(LO_1) = \begin{bmatrix} -0.079 - 0.345i & -0.013 - 0.294i & 0.005 + 0.126i \\ -0.049 + 0.300i & -0.019 + 0.230i & -0.018 + 0.009i \\ 0.050 - 0.347i & -0.062 - 0.299i & -0.015 - 0.126i \\ 0.064 + 0.299i & 0.090 + 0.229i & -0.007 - 0.008i \\ 0.048 + 0.330i & -0.011 + 0.041i & -0.088 + 0.006i \\ 0.015 - 0.025i & 0.026 + 0.334i & 0.081 + 0.000i \end{bmatrix}$$

$$\boldsymbol{u}(LO_5) = \begin{bmatrix} -0.098 + 0.004i & 0.043 - 0.001i & 0.069 - 0.003i \\ -0.105 - 0.001i & -0.055 - 0.001i & -0.063 - 0.002i \\ -0.101 + 0.003i & 0.046 - 0.002i & -0.069 + 0.003i \\ -0.108 + 0.010i & -0.058 + 0.006i & 0.063 - 0.007i \\ 0.574 - 0.057i & 0.368 - 0.039i & -0.011 + 0.002i \\ 0.607 - 0.024i & -0.300 + 0.009i & 0.005 + 0.000i \end{bmatrix}$$

$$\boldsymbol{u}(LO_2) = \begin{bmatrix} -0.330 + 0.019i & -0.329 + 0.026i & 0.179 - 0.010i \\ -0.330 - 0.002i & 0.330 - 0.006i & -0.179 - 0.001i \\ 0.330 + 0.013i & 0.330 + 0.021i & 0.177 + 0.007i \\ 0.330 - 0.007i & -0.331 + 0.000i & -0.178 + 0.004i \\ 0.001 + 0.005i & 0.000 + 0.002i & 0.000 - 0.000i \\ 0.000 + 0.005i & 0.000 - 0.002i & 0.000 + 0.000i \end{bmatrix}$$

$$\boldsymbol{u}(LO_3) = \begin{bmatrix} -0.351 + 0.021i & -0.351 + 0.021i & -0.011 + 0.003i \\ 0.352 + 0.001i & -0.352 - 0.001i & -0.011 + 0.003i \\ 0.351 + 0.021i & 0.351 + 0.021i & -0.010 - 0.003i \\ -0.352 + 0.001i & 0.352 - 0.001i & -0.011 - 0.003i \\ 0.000 - 0.006i & 0.000 + 0.000i & 0.061 - 0.004i \\ 0.000 + 0.006i & 0.000 + 0.000i & 0.062 + 0.000i \end{bmatrix}$$

$$\boldsymbol{u}(LO_4) = \begin{bmatrix} 0.011 - 0.076i & -0.006 + 0.056i & -0.015 + 0.094i \\ -0.018 + 0.075i & -0.013 + 0.058i & -0.015 + 0.088i \\ 0.009 - 0.076i & -0.007 + 0.056i & 0.016 - 0.094i \\ -0.006 + 0.077i & -0.007 + 0.058i & 0.005 - 0.089i \\ 0.054 - 0.595i & 0.011 - 0.314i & 0.001 + 0.000i \\ -0.077 + 0.587i & 0.063 - 0.343i & 0.001 + 0.000i \end{bmatrix}$$

II. Penta-Bi_2Sn Monolayer

$$\boldsymbol{u}(ZO_3) = \begin{bmatrix} 0.029 + 0.026i & 0.072 + 0.114i & 0.255 + 0.371i \\ 0.021 + 0.019i & -0.063 - 0.115i & -0.200 - 0.335i \\ 0.012 + 0.038i & 0.073 + 0.108i & -0.233 - 0.384i \\ 0.008 + 0.026i & -0.078 - 0.102i & 0.224 + 0.318i \\ -0.055 - 0.073i & -0.188 - 0.253i & -0.001 + 0.000i \\ -0.075 - 0.116i & 0.165 + 0.254i & 0.003 + 0.000i \end{bmatrix}$$

$$\boldsymbol{u}(\mathrm{TO}_1) = \begin{bmatrix} 0.043 + 0.106i & -0.096 - 0.348i & 0.018 + 0.051i \\ -0.048 - 0.221i & 0.096 + 0.401i & -0.022 - 0.127i \\ 0.025 + 0.109i & -0.046 - 0.354i & 0.001 - 0.056i \\ -0.068 - 0.218i & 0.076 + 0.403i & 0.036 + 0.123i \\ 0.020 + 0.101i & -0.094 - 0.317i & 0.013 - 0.002i \\ 0.069 + 0.299i & 0.024 + 0.145i & -0.010 + 0.000i \end{bmatrix}$$

$$\boldsymbol{u}(LO_4) = \begin{bmatrix} 0.004 - 0.030i & -0.003 - 0.045i & 0.006 + 0.141i \\ -0.008 + 0.044i & -0.000 - 0.055i & -0.006 + 0.185i \\ -0.004 - 0.030i & 0.004 - 0.045i & 0.007 - 0.141i \\ 0.006 + 0.044i & 0.001 - 0.055i & -0.002 - 0.185i \\ -0.035 - 0.656i & 0.007 + 0.090i & -0.008 + 0.000i \\ -0.003 + 0.606i & -0.004 + 0.261i & -0.006 + 0.000i \end{bmatrix}$$

$$\boldsymbol{u}(LO_5) = \begin{bmatrix} -0.023 + 0.090i & -0.001 + 0.011i & 0.037 - 0.168i \\ -0.027 + 0.085i & -0.003 + 0.009i & -0.038 + 0.124i \\ -0.023 + 0.094i & -0.004 + 0.009i & -0.047 + 0.165i \\ -0.018 + 0.092i & -0.001 + 0.011i & 0.028 - 0.128i \\ 0.048 - 0.243i & 0.112 - 0.591i & -0.011 + 0.005i \\ 0.099 - 0.396i & -0.132 + 0.514i & 0.012 + 0.000i \end{bmatrix}$$

$$\boldsymbol{u}(LO_1) = \begin{bmatrix} -0.029 - 0.411i & -0.023 - 0.228i & -0.005 + 0.123i \\ 0.010 + 0.361i & -0.013 + 0.111i & -0.010 + 0.048i \\ -0.001 - 0.412i & 0.027 - 0.229i & -0.010 - 0.122i \\ 0.023 + 0.360i & -0.002 + 0.110i & -0.020 - 0.047i \\ 0.027 + 0.323i & 0.018 + 0.105i & 0.001 + 0.000i \\ -0.012 - 0.140i & 0.005 + 0.312i & -0.008 + 0.000i \end{bmatrix}$$

$$\boldsymbol{u}(LO_2) = \begin{bmatrix} -0.342 - 0.049i & -0.341 - 0.042i & 0.114 + 0.018i \\ -0.338 - 0.070i & 0.337 + 0.063i & -0.113 - 0.025i \\ 0.334 + 0.082i & 0.334 + 0.089i & 0.110 + 0.025i \\ 0.338 + 0.060i & -0.339 - 0.067i & -0.112 - 0.018i \\ 0.002 + 0.007i & 0.000 + 0.004i & 0.001 + 0.000i \\ 0.001 + 0.007i & 0.001 - 0.004i & 0.000 + 0.000i \end{bmatrix}$$

A III.3 CALCULATED MACROSCOPIC POLARIZATIONS

The macroscopic electric polarization induced by a specific optical phonon mode is rigorously defined by the linear combination of the product between the Born effective charge tensors (Z^*) and the corresponding normalized atomic displacement vectors (u). This formulation accounts for the site-specific electronic responses and local symmetries of the Bi and Ge/Sn atoms within the penta-atomic unit cell. The resulting vector represents the net dipole moment per unit cell generated by the collective lattice dynamics.

(I) Penta-Bi_2Ge Monolayer

$$\boldsymbol{P}(ZO_3) = \boldsymbol{Z}^*_{\boldsymbol{Bi}\,(1)}\boldsymbol{u}_{\mathrm{Bi}\,(1)} + \boldsymbol{Z}^*_{\boldsymbol{Bi}\,(2)}\boldsymbol{u}_{\mathrm{Bi}\,(2)} + \boldsymbol{Z}^*_{\boldsymbol{Bi}\,(3)}\boldsymbol{u}_{\mathrm{Bi}\,(3)} + \boldsymbol{Z}^*_{\boldsymbol{Bi}\,(4)}\boldsymbol{u}_{\mathrm{Bi}\,(4)} + \boldsymbol{Z}^*_{\boldsymbol{Ge}\,(1)}\boldsymbol{u}_{\mathrm{Ge}\,(1)} +$$

$$\boldsymbol{Z}^*_{\boldsymbol{Ge}\,(2)}\boldsymbol{u}_{\mathrm{Ge}\,(2)} = \begin{bmatrix} -0.524 & -0.448 & -0.541 \\ -0.448 & -0.524 & -0.541 \\ 0.020 & 0.020 & -0.001 \end{bmatrix} \begin{bmatrix} -0.030 + 0.011i \\ -0.119 - 0.011i \\ -0.474 - 0.005i \end{bmatrix} +$$

$$\begin{bmatrix} -0.524 & 0.448 & 0.541 \\ 0.448 & -0.524 & -0.541 \\ -0.020 & 0.020 & -0.001 \end{bmatrix} \begin{bmatrix} -0.002 + 0.007i \\ 0.113 + 0.017i \\ 0.337 + 0.027i \end{bmatrix} +$$

$$\begin{bmatrix} -0.524 & -0.448 & 0.541 \\ -0.448 & -0.524 & 0.541 \\ -0.020 & -0.020 & -0.001 \end{bmatrix} \begin{bmatrix} -0.033 - 0.013i \\ -0.113 + 0.003i \\ 0.472 + 0.033i \end{bmatrix} +$$

$$\begin{bmatrix} -0.524 & 0.448 & -0.541 \\ 0.448 & -0.524 & 0.541 \\ 0.020 & -0.020 & -0.001 \end{bmatrix} \begin{bmatrix} -0.005 - 0.008i \\ 0.108 - 0.008i \\ -0.337 + 0.000i \end{bmatrix} +$$

$$\begin{bmatrix} 1.049 & 0.528 & 0.000 \\ -0.528 & 1.049 & 0.000 \\ 0.000 & 0.000 & 0.002 \end{bmatrix} \begin{bmatrix} 0.043 - 0.001i \\ 0.361 - 0.009i \\ 0.002 + 0.002i \end{bmatrix} +$$

$$\begin{bmatrix} 1.049 & -0.528 & 0.000 \\ 0.528 & 1.049 & 0.000 \\ 0.000 & 0.000 & 0.002 \end{bmatrix} \begin{bmatrix} 0.163 + 0.006i \\ -0.331 - 0.013i \\ -0.004 + 0.000i \end{bmatrix} = \boldsymbol{P}^{\boldsymbol{total}}_{\boldsymbol{x}} + \boldsymbol{P}^{\boldsymbol{total}}_{\boldsymbol{y}} + \boldsymbol{P}^{\boldsymbol{total}}_{\boldsymbol{z}} =$$

$$\begin{bmatrix} 0.253 + 0.007i \\ 0.088 + 0.004i \\ 0.000 + 0.000i \end{bmatrix} + \begin{bmatrix} 0.568 + 0.010i \\ 0.037 - 0.024i \\ 0.000 + 0.000i \end{bmatrix} + \begin{bmatrix} 0.876 + 0.035i \\ 0.147 + 0.006i \\ 0.000 - 0.000i \end{bmatrix} =$$

$$\begin{bmatrix} 1.698 + 0.052i \\ 0.273 - 0.014i \\ 0.000 + 0.000i \end{bmatrix} e\,\text{Å} \quad u.c.^{-1}$$

$$\begin{aligned} \boldsymbol{P}(LO_1) &= \boldsymbol{Z}^*_{\boldsymbol{Bi(1)}}\boldsymbol{u}_{\text{Bi (1)}} + \boldsymbol{Z}^*_{\boldsymbol{Bi(2)}}\boldsymbol{u}_{\text{Bi (2)}} + \boldsymbol{Z}^*_{\boldsymbol{Bi(3)}}\boldsymbol{u}_{\text{Bi (3)}} + \boldsymbol{Z}^*_{\boldsymbol{Bi(4)}}\boldsymbol{u}_{\text{Bi (4)}} + \boldsymbol{Z}^*_{\boldsymbol{Ge(1)}}\boldsymbol{u}_{\text{Ge (1)}} \\ &\quad + \boldsymbol{Z}^*_{\boldsymbol{Ge(2)}}\boldsymbol{u}_{\text{Ge (2)}} \\ &= \begin{bmatrix} -0.524 & -0.448 & -0.541 \\ -0.448 & -0.524 & -0.541 \\ 0.020 & 0.020 & -0.001 \end{bmatrix} \begin{bmatrix} -0.079 - 0.345i \\ -0.013 - 0.294i \\ 0.005 + 0.126i \end{bmatrix} \\ &\quad + \begin{bmatrix} -0.524 & 0.448 & 0.541 \\ 0.448 & -0.524 & -0.541 \\ -0.020 & 0.020 & -0.001 \end{bmatrix} \begin{bmatrix} -0.049 + 0.300i \\ -0.019 + 0.230i \\ -0.018 + 0.009i \end{bmatrix} \\ &\quad + \begin{bmatrix} -0.524 & -0.448 & 0.541 \\ -0.448 & -0.524 & 0.541 \\ -0.020 & -0.020 & -0.001 \end{bmatrix} \begin{bmatrix} 0.050 - 0.347i \\ -0.062 - 0.299i \\ -0.015 - 0.126i \end{bmatrix} \\ &\quad + \begin{bmatrix} -0.524 & 0.448 & -0.541 \\ 0.448 & -0.524 & 0.541 \\ 0.020 & -0.020 & -0.001 \end{bmatrix} \begin{bmatrix} 0.064 + 0.299i \\ 0.090 + 0.229i \\ -0.007 - 0.008i \end{bmatrix} \\ &\quad + \begin{bmatrix} 1.049 & 0.528 & 0.000 \\ -0.528 & 1.049 & 0.000 \\ 0.000 & 0.000 & 0.002 \end{bmatrix} \begin{bmatrix} 0.048 + 0.330i \\ -0.011 + 0.041i \\ -0.088 + 0.006i \end{bmatrix} \\ &\quad + \begin{bmatrix} 1.049 & -0.528 & 0.000 \\ 0.528 & 1.049 & 0.000 \\ 0.000 & 0.000 & 0.002 \end{bmatrix} \begin{bmatrix} 0.015 - 0.025i \\ 0.026 + 0.034i \\ 0.081 + 0.000i \end{bmatrix} = \boldsymbol{P}^{\boldsymbol{total}}_{\boldsymbol{x}} + \boldsymbol{P}^{\boldsymbol{total}}_{\boldsymbol{y}} + \boldsymbol{P}^{\boldsymbol{total}}_{\boldsymbol{z}} \\ &= \begin{bmatrix} 0.073 + 0.369i \\ 0.002 + 0.391i \\ -0.000 + 0.000i \end{bmatrix} + \begin{bmatrix} 0.046 + 0.317i \\ 0.018 + 0.464i \\ -0.001 + 0.000i \end{bmatrix} + \begin{bmatrix} -0.017 - 0.127i \\ -0.005 - 0.146i \\ 0.000 + 0.000i \end{bmatrix} \\ &= \begin{bmatrix} 0.103 + 0.558i \\ 0.015 + 0.709i \\ -0.001 + 0.000i \end{bmatrix} e\,\text{Å} \quad u.c.^{-1} \end{aligned}$$

$$
\begin{aligned}
\boldsymbol{P}(LO_5) &= \boldsymbol{Z}^{*}_{\boldsymbol{Bi(1)}}\boldsymbol{u}_{\mathrm{Bi\,(1)}} + \boldsymbol{Z}^{*}_{\boldsymbol{Bi(2)}}\boldsymbol{u}_{\mathrm{Bi\,(2)}} + \boldsymbol{Z}^{*}_{\boldsymbol{Bi(3)}}\boldsymbol{u}_{\mathrm{Bi\,(3)}} + \boldsymbol{Z}^{*}_{\boldsymbol{Bi(4)}}\boldsymbol{u}_{\mathrm{Bi\,(4)}} + \boldsymbol{Z}^{*}_{\boldsymbol{Ge(1)}}\boldsymbol{u}_{\mathrm{Ge\,(1)}} \\
&\quad + \boldsymbol{Z}^{*}_{\boldsymbol{Ge(2)}}\boldsymbol{u}_{\mathrm{Ge\,(2)}} \\
&= \begin{bmatrix} -0.524 & -0.448 & -0.541 \\ -0.448 & -0.524 & -0.541 \\ 0.020 & 0.020 & -0.001 \end{bmatrix}\begin{bmatrix} -0.098 + 0.004i \\ 0.043 - 0.001i \\ 0.069 - 0.003i \end{bmatrix} \\
&\quad + \begin{bmatrix} -0.524 & 0.448 & 0.541 \\ 0.448 & -0.524 & -0.541 \\ -0.020 & 0.020 & -0.001 \end{bmatrix}\begin{bmatrix} -0.105 - 0.001i \\ -0.055 - 0.001i \\ -0.063 - 0.002i \end{bmatrix} \\
&\quad + \begin{bmatrix} -0.524 & -0.448 & 0.541 \\ -0.448 & -0.524 & 0.541 \\ -0.020 & -0.020 & -0.001 \end{bmatrix}\begin{bmatrix} -0.101 + 0.003i \\ 0.046 - 0.002i \\ -0.069 + 0.003i \end{bmatrix} \\
&\quad + \begin{bmatrix} -0.524 & 0.448 & -0.541 \\ 0.448 & -0.524 & 0.541 \\ 0.020 & -0.020 & -0.001 \end{bmatrix}\begin{bmatrix} -0.108 + 0.010i \\ -0.058 + 0.006i \\ 0.063 - 0.007i \end{bmatrix} \\
&\quad + \begin{bmatrix} 1.049 & 0.528 & 0.000 \\ -0.528 & 1.049 & 0.000 \\ 0.000 & 0.000 & 0.002 \end{bmatrix}\begin{bmatrix} 0.574 - 0.057i \\ 0.368 - 0.039i \\ -0.011 + 0.002i \end{bmatrix} \\
&\quad + \begin{bmatrix} 1.049 & -0.528 & 0.000 \\ 0.528 & 1.049 & 0.000 \\ 0.000 & 0.000 & 0.002 \end{bmatrix}\begin{bmatrix} 0.607 - 0.024i \\ -0.300 + 0.009i \\ 0.005 + 0.000i \end{bmatrix} = \boldsymbol{P}_{\boldsymbol{x}}^{\boldsymbol{total}} + \boldsymbol{P}_{\boldsymbol{y}}^{\boldsymbol{total}} + \boldsymbol{P}_{\boldsymbol{z}}^{\boldsymbol{total}} \\
&= \begin{bmatrix} 1.455 - 0.093i \\ 0.011 + 0.018i \\ 0.000 + 0.000i \end{bmatrix} + \begin{bmatrix} 0.262 - 0.022i \\ 0.084 - 0.032i \\ 0.000 + 0.000i \end{bmatrix} + \begin{bmatrix} -0.143 + 0.006i \\ -0.006 + 0.001i \\ 0.000 + 0.000i \end{bmatrix} \\
&= \begin{bmatrix} 1.574 - 0.110i \\ 0.089 - 0.014i \\ 0.000 + 0.000i \end{bmatrix} e\,\text{Å} \quad u.c.^{-1}
\end{aligned}
$$

$$
\begin{aligned}
\boldsymbol{P}(LO_2) \;=\; & \boldsymbol{Z^*_{Bi(1)}}\boldsymbol{u}_{\mathrm{Bi\,(1)}} + \boldsymbol{Z^*_{Bi(2)}}\boldsymbol{u}_{\mathrm{Bi\,(2)}} + \boldsymbol{Z^*_{Bi(3)}}\boldsymbol{u}_{\mathrm{Bi\,(3)}} + \boldsymbol{Z^*_{Bi(4)}}\boldsymbol{u}_{\mathrm{Bi\,(4)}} + \boldsymbol{Z^*_{Ge(1)}}\boldsymbol{u}_{\mathrm{Ge\,(1)}} \\
& + \boldsymbol{Z^*_{Ge(2)}}\boldsymbol{u}_{\mathrm{Ge\,(2)}} \\
= & \begin{bmatrix} -0.524 & -0.448 & -0.541 \\ -0.448 & -0.524 & -0.541 \\ 0.020 & 0.020 & -0.001 \end{bmatrix} \begin{bmatrix} -0.330 + 0.019i \\ -0.329 + 0.026i \\ 0.179 - 0.010i \end{bmatrix} \\
& + \begin{bmatrix} -0.524 & 0.448 & 0.541 \\ 0.448 & -0.524 & -0.541 \\ -0.020 & 0.020 & -0.001 \end{bmatrix} \begin{bmatrix} -0.330 - 0.002i \\ 0.330 - 0.006i \\ -0.179 - 0.001i \end{bmatrix} \\
& + \begin{bmatrix} -0.524 & -0.448 & 0.541 \\ -0.448 & -0.524 & 0.541 \\ -0.020 & -0.020 & -0.001 \end{bmatrix} \begin{bmatrix} 0.330 + 0.013i \\ 0.330 + 0.021i \\ 0.177 + 0.007i \end{bmatrix} \\
& + \begin{bmatrix} -0.524 & 0.448 & -0.541 \\ 0.448 & -0.524 & 0.541 \\ 0.020 & -0.020 & -0.001 \end{bmatrix} \begin{bmatrix} 0.330 - 0.007i \\ -0.331 + 0.000i \\ -0.178 + 0.004i \end{bmatrix} \\
& + \begin{bmatrix} 1.049 & 0.528 & 0.000 \\ -0.528 & 1.049 & 0.000 \\ 0.000 & 0.000 & 0.002 \end{bmatrix} \begin{bmatrix} 0.001 + 0.005i \\ 0.000 + 0.002i \\ 0.000 - 0.000i \end{bmatrix} \\
& + \begin{bmatrix} 1.049 & -0.528 & 0.000 \\ 0.528 & 1.049 & 0.000 \\ 0.000 & 0.000 & 0.002 \end{bmatrix} \begin{bmatrix} 0.000 + 0.005i \\ 0.000 - 0.002i \\ -0.000 + 0.000i \end{bmatrix} = \boldsymbol{P_x^{total}} + \boldsymbol{P_y^{total}} + \boldsymbol{P_z^{total}} \\
= & \begin{bmatrix} 0.002 - 0.002i \\ -0.000 - 0.018i \\ 0.000 - 0.000i \end{bmatrix} + \begin{bmatrix} -0.001 - 0.021i \\ 0.000 - 0.022i \\ 0.000 - 0.000i \end{bmatrix} + \begin{bmatrix} -0.001 + 0.007i \\ -0.000 + 0.012i \\ 0.000 + 0.000i \end{bmatrix} \\
= & \begin{bmatrix} -0.001 - 0.016i \\ -0.000 - 0.028i \\ 0.000 - 0.000i \end{bmatrix} e\,\text{Å} \quad u.c.^{-1}
\end{aligned}
$$

$$
\begin{aligned}
\boldsymbol{P}(LO_3) \;=\; & \boldsymbol{Z}^{*}_{\boldsymbol{Bi(1)}}\boldsymbol{u}_{\mathrm{Bi\,(1)}} + \boldsymbol{Z}^{*}_{\boldsymbol{Bi(2)}}\boldsymbol{u}_{\mathrm{Bi\,(2)}} + \boldsymbol{Z}^{*}_{\boldsymbol{Bi(3)}}\boldsymbol{u}_{\mathrm{Bi\,(3)}} + \boldsymbol{Z}^{*}_{\boldsymbol{Bi(4)}}\boldsymbol{u}_{\mathrm{Bi\,(4)}} + \boldsymbol{Z}^{*}_{\boldsymbol{Ge(1)}}\boldsymbol{u}_{\mathrm{Ge\,(1)}} \\
& + \boldsymbol{Z}^{*}_{\boldsymbol{Ge(2)}}\boldsymbol{u}_{\mathrm{Ge\,(2)}} \\
= & \begin{bmatrix} -0.524 & -0.448 & -0.541 \\ -0.448 & -0.524 & -0.541 \\ 0.020 & 0.020 & -0.001 \end{bmatrix} \begin{bmatrix} -0.351 + 0.021i \\ -0.351 + 0.021i \\ -0.011 + 0.003i \end{bmatrix} \\
& + \begin{bmatrix} -0.524 & 0.448 & 0.541 \\ 0.448 & -0.524 & -0.541 \\ -0.020 & 0.020 & -0.001 \end{bmatrix} \begin{bmatrix} 0.352 + 0.001i \\ -0.352 - 0.001i \\ -0.011 + 0.003i \end{bmatrix} \\
& + \begin{bmatrix} -0.524 & -0.448 & 0.541 \\ -0.448 & -0.524 & 0.541 \\ -0.020 & -0.020 & -0.001 \end{bmatrix} \begin{bmatrix} 0.351 + 0.021i \\ 0.351 + 0.021i \\ -0.010 - 0.003i \end{bmatrix} \\
& + \begin{bmatrix} -0.524 & 0.448 & -0.541 \\ 0.448 & -0.524 & 0.541 \\ 0.020 & -0.020 & -0.001 \end{bmatrix} \begin{bmatrix} -0.352 + 0.001i \\ -0.352 + 0.001i \\ -0.011 - 0.003i \end{bmatrix} \\
& + \begin{bmatrix} 1.049 & 0.528 & 0.000 \\ -0.528 & 1.049 & 0.000 \\ 0.000 & 0.000 & 0.002 \end{bmatrix} \begin{bmatrix} -0.000 - 0.006i \\ -0.000 + 0.000i \\ 0.061 - 0.004i \end{bmatrix} \\
& + \begin{bmatrix} 1.049 & -0.528 & 0.000 \\ 0.528 & 1.049 & 0.000 \\ 0.000 & 0.000 & 0.002 \end{bmatrix} \begin{bmatrix} -0.000 + 0.006i \\ -0.000 + 0.000i \\ 0.062 + 0.000i \end{bmatrix} = \boldsymbol{P}_{\boldsymbol{x}}^{\boldsymbol{total}} + \boldsymbol{P}_{\boldsymbol{y}}^{\boldsymbol{total}} + \boldsymbol{P}_{\boldsymbol{z}}^{\boldsymbol{total}} \\
= & \begin{bmatrix} -0.001 - 0.023i \\ 0.000 - 0.012i \\ -0.028 + 0.000i \end{bmatrix} + \begin{bmatrix} 0.000 - 0.020i \\ -0.000 - 0.020i \\ -0.028 + 0.000i \end{bmatrix} + \begin{bmatrix} 0.000 - 0.001i \\ 0.000 - 0.007i \\ 0.000 - 0.000i \end{bmatrix} \\
= & \begin{bmatrix} -0.000 - 0.044i \\ 0.000 - 0.038i \\ -0.056 + 0.000i \end{bmatrix} e\,\text{Å} \quad u.c.^{-1}
\end{aligned}
$$

$$
\begin{aligned}
\boldsymbol{P}(LO_4) \;=\; & \boldsymbol{Z^{*}_{Bi(1)}}\boldsymbol{u}_{\text{Bi (1)}} + \boldsymbol{Z^{*}_{Bi(2)}}\boldsymbol{u}_{\text{Bi (2)}} + \boldsymbol{Z^{*}_{Bi(3)}}\boldsymbol{u}_{\text{Bi (3)}} + \boldsymbol{Z^{*}_{Bi(4)}}\boldsymbol{u}_{\text{Bi (4)}} + \boldsymbol{Z^{*}_{Ge(1)}}\boldsymbol{u}_{\text{Ge (1)}} \\
& + \boldsymbol{Z^{*}_{Ge(2)}}\boldsymbol{u}_{\text{Ge (2)}} \\
= & \begin{bmatrix} -0.524 & -0.448 & -0.541 \\ -0.448 & -0.524 & -0.541 \\ 0.020 & 0.020 & -0.001 \end{bmatrix} \begin{bmatrix} 0.011 - 0.076i \\ -0.006 + 0.056i \\ -0.015 + 0.094i \end{bmatrix} \\
& + \begin{bmatrix} -0.524 & 0.448 & 0.541 \\ 0.448 & -0.524 & -0.541 \\ -0.020 & 0.020 & -0.001 \end{bmatrix} \begin{bmatrix} -0.018 + 0.075i \\ -0.013 + 0.058i \\ -0.015 + 0.088i \end{bmatrix} \\
& + \begin{bmatrix} -0.524 & -0.448 & 0.541 \\ -0.448 & -0.524 & 0.541 \\ -0.020 & -0.020 & -0.001 \end{bmatrix} \begin{bmatrix} 0.009 - 0.076i \\ -0.007 + 0.056i \\ 0.016 - 0.094i \end{bmatrix} \\
& + \begin{bmatrix} -0.524 & 0.448 & -0.541 \\ 0.448 & -0.524 & 0.541 \\ 0.020 & -0.020 & -0.001 \end{bmatrix} \begin{bmatrix} -0.006 + 0.077i \\ -0.007 + 0.058i \\ 0.005 - 0.089i \end{bmatrix} \\
& + \begin{bmatrix} 1.049 & 0.528 & 0.000 \\ -0.528 & 1.049 & 0.000 \\ 0.000 & 0.000 & 0.002 \end{bmatrix} \begin{bmatrix} 0.054 - 0.595i \\ 0.011 - 0.314i \\ 0.001 + 0.000i \end{bmatrix} \\
& + \begin{bmatrix} 1.049 & -0.528 & 0.000 \\ 0.528 & 1.049 & 0.000 \\ 0.000 & 0.000 & 0.002 \end{bmatrix} \begin{bmatrix} -0.077 + 0.587i \\ 0.063 - 0.443i \\ 0.001 + 0.000i \end{bmatrix} = \boldsymbol{P_x^{total}} + \boldsymbol{P_y^{total}} + \boldsymbol{P_z^{total}} \\
= & \begin{bmatrix} -0.021 - 0.009i \\ -0.088 + 0.761i \\ 0.000 + 0.000i \end{bmatrix} + \begin{bmatrix} -0.031 + 0.017i \\ 0.095 - 0.809i \\ -0.000 - 0.000i \end{bmatrix} + \begin{bmatrix} 0.005 - 0.006i \\ 0.028 - 0.197i \\ 0.000 + 0.000i \end{bmatrix} \\
= & \begin{bmatrix} -0.046 + 0.003i \\ 0.034 - 0.246i \\ 0.000 + 0.000i \end{bmatrix} e\,\text{Å} \quad u.c.^{-1}
\end{aligned}
$$

(II). Penta-Bi_2Sn Monolayer

$$
\begin{aligned}
\boldsymbol{P}(ZO_3) &= \boldsymbol{Z}^*_{\boldsymbol{Bi(1)}}\boldsymbol{u}_{\mathrm{Bi\ (1)}} + \boldsymbol{Z}^*_{\boldsymbol{Bi(2)}}\boldsymbol{u}_{\mathrm{Bi\ (2)}} + \boldsymbol{Z}^*_{\boldsymbol{Bi(3)}}\boldsymbol{u}_{\mathrm{Bi\ (3)}} + \boldsymbol{Z}^*_{\boldsymbol{Bi(4)}}\boldsymbol{u}_{\mathrm{Bi\ (4)}} \\
&+ \boldsymbol{Z}^*_{\boldsymbol{Sn(1)}}\boldsymbol{u}_{\mathrm{Sn\ (1)}} + \boldsymbol{Z}^*_{\boldsymbol{Sn(2)}}\boldsymbol{u}_{\mathrm{Sn\ (2)}} \\
&= \begin{bmatrix} -0.798 & -0.143 & -0.424 \\ -0.143 & -0.798 & -0.424 \\ 0.020 & 0.020 & -0.018 \end{bmatrix}\begin{bmatrix} 0.029 + 0.026i \\ 0.072 + 0.114i \\ 0.255 + 0.371i \end{bmatrix} \\
&+ \begin{bmatrix} -0.798 & 0.143 & 0.424 \\ 0.143 & -0.798 & -0.424 \\ -0.020 & 0.020 & -0.018 \end{bmatrix}\begin{bmatrix} 0.021 + 0.019i \\ -0.063 - 0.115i \\ -0.200 - 0.335i \end{bmatrix} \\
&+ \begin{bmatrix} -0.798 & -0.143 & 0.424 \\ -0.143 & -0.798 & 0.424 \\ -0.020 & -0.020 & -0.018 \end{bmatrix}\begin{bmatrix} 0.012 + 0.038i \\ 0.073 + 0.108i \\ -0.233 - 0.384i \end{bmatrix} \\
&+ \begin{bmatrix} -0.798 & 0.143 & -0.424 \\ 0.143 & -0.798 & 0.424 \\ 0.020 & -0.020 & -0.018 \end{bmatrix}\begin{bmatrix} 0.008 + 0.026i \\ -0.078 - 0.102i \\ 0.224 + 0.318i \end{bmatrix} \\
&+ \begin{bmatrix} 1.597 & 0.500 & 0.000 \\ -0.500 & 1.597 & 0.000 \\ 0.000 & 0.000 & 0.036 \end{bmatrix}\begin{bmatrix} -0.055 - 0.073i \\ -0.188 - 0.253i \\ -0.001 + 0.000i \end{bmatrix} \\
&+ \begin{bmatrix} 1.597 & -0.500 & 0.000 \\ 0.500 & 1.597 & 0.000 \\ 0.000 & 0.000 & 0.036 \end{bmatrix}\begin{bmatrix} -0.075 - 0.116i \\ 0.165 + 0.254i \\ 0.003 + 0.000i \end{bmatrix} \\
&= \boldsymbol{P}^{\boldsymbol{total}}_{\boldsymbol{x}} + \boldsymbol{P}^{\boldsymbol{total}}_{\boldsymbol{y}} + \boldsymbol{P}^{\boldsymbol{total}}_{\boldsymbol{z}} \\
&= \begin{bmatrix} -0.263 - 0.390i \\ -0.012 - 0.024i \\ 0.000 - 0.000i \end{bmatrix} + \begin{bmatrix} -0.217 - 0.317i \\ 0.040 - 0.004i \\ 0.000 - 0.000i \end{bmatrix} \\
&+ \begin{bmatrix} -0.387 - 0.597i \\ -0.027 - 0.043i \\ -0.001 + 0.001i \end{bmatrix} = \begin{bmatrix} -0.867 - 1.303i \\ -0.078 - 0.072i \\ -0.000 + 0.000i \end{bmatrix} e\ \text{Å} \quad u.c.^{-1}
\end{aligned}
$$

$$
\begin{aligned}
\boldsymbol{P}(TO_1) = {} & \boldsymbol{Z}^*_{\boldsymbol{Bi(1)}}\boldsymbol{u}_{\text{Bi }(\mathbf{1})} + \boldsymbol{Z}^*_{\boldsymbol{Bi(2)}}\boldsymbol{u}_{\text{Bi }(\mathbf{2})} + \boldsymbol{Z}^*_{\boldsymbol{Bi(3)}}\boldsymbol{u}_{\text{Bi }(\mathbf{3})} + \boldsymbol{Z}^*_{\boldsymbol{Bi(4)}}\boldsymbol{u}_{\text{Bi }(\mathbf{4})} \\
& + \boldsymbol{Z}^*_{\boldsymbol{Sn(1)}}\boldsymbol{u}_{\text{Sn }(\mathbf{1})} + \boldsymbol{Z}^*_{\boldsymbol{Sn(2)}}\boldsymbol{u}_{\text{Sn }(\mathbf{2})} \\
= {} & \begin{bmatrix} -0.798 & -0.143 & -0.424 \\ -0.143 & -0.798 & -0.424 \\ 0.020 & 0.020 & -0.018 \end{bmatrix} \begin{bmatrix} 0.043 + 0.106i \\ -0.096 - 0.348i \\ 0.018 + 0.051i \end{bmatrix} \\
& + \begin{bmatrix} -0.798 & 0.143 & 0.424 \\ 0.143 & -0.798 & -0.424 \\ -0.020 & 0.020 & -0.018 \end{bmatrix} \begin{bmatrix} -0.048 - 0.221i \\ 0.096 + 0.401i \\ -0.022 - 0.127i \end{bmatrix} \\
& + \begin{bmatrix} -0.798 & -0.143 & 0.424 \\ -0.143 & -0.798 & 0.424 \\ -0.020 & -0.020 & -0.018 \end{bmatrix} \begin{bmatrix} 0.025 + 0.109i \\ -0.046 - 0.354i \\ 0.001 - 0.056i \end{bmatrix} \\
& + \begin{bmatrix} -0.798 & 0.143 & -0.424 \\ 0.143 & -0.798 & 0.424 \\ 0.020 & -0.020 & -0.018 \end{bmatrix} \begin{bmatrix} -0.068 - 0.218i \\ 0.076 + 0.403i \\ 0.036 + 0.123i \end{bmatrix} \\
& + \begin{bmatrix} 1.597 & 0.500 & 0.000 \\ -0.500 & 1.597 & 0.000 \\ 0.000 & 0.000 & 0.036 \end{bmatrix} \begin{bmatrix} 0.020 + 0.101i \\ -0.094 - 0.317i \\ 0.013 - 0.002i \end{bmatrix} \\
& + \begin{bmatrix} 1.597 & -0.500 & 0.000 \\ 0.500 & 1.597 & 0.000 \\ 0.000 & 0.000 & 0.036 \end{bmatrix} \begin{bmatrix} 0.069 + 0.299i \\ 0.024 + 0.145i \\ -0.010 + 0.000i \end{bmatrix} \\
= {} & \boldsymbol{P}^{\boldsymbol{total}}_{\boldsymbol{x}} + \boldsymbol{P}^{\boldsymbol{total}}_{\boldsymbol{y}} + \boldsymbol{P}^{\boldsymbol{total}}_{\boldsymbol{z}} \\
= {} & \begin{bmatrix} 0.181 + 0.818i \\ -0.002 + 0.005i \\ -0.000 + 0.000i \end{bmatrix} + \begin{bmatrix} -0.014 - 0.016i \\ -0.135 - 0.358i \\ -0.001 + 0.000i \end{bmatrix} \\
& + \begin{bmatrix} -0.032 - 0.151i \\ 0.017 + 0.061i \\ -0.000 + 0.000i \end{bmatrix} = \begin{bmatrix} 0.135 + 0.650i \\ -0.120 - 0.292i \\ -0.001 + 0.000i \end{bmatrix} e\,\text{Å} \quad u.c.^{-1}
\end{aligned}
$$

$$
\begin{aligned}
\boldsymbol{P}(LO_4) \;=\; & \boldsymbol{Z}^{*}_{\boldsymbol{Bi(1)}}\boldsymbol{u}_{\mathrm{Bi\ (1)}} + \boldsymbol{Z}^{*}_{\boldsymbol{Bi(2)}}\boldsymbol{u}_{\mathrm{Bi\ (2)}} + \boldsymbol{Z}^{*}_{\boldsymbol{Bi(3)}}\boldsymbol{u}_{\mathrm{Bi\ (3)}} + \boldsymbol{Z}^{*}_{\boldsymbol{Bi(4)}}\boldsymbol{u}_{\mathrm{Bi\ (4)}} \\
& + \boldsymbol{Z}^{*}_{\boldsymbol{Sn(1)}}\boldsymbol{u}_{\mathrm{Sn\ (1)}} + \boldsymbol{Z}^{*}_{\boldsymbol{Sn(2)}}\boldsymbol{u}_{\mathrm{Sn\ (2)}} \\
& = \begin{bmatrix} -0.798 & -0.143 & -0.424 \\ -0.143 & -0.798 & -0.424 \\ 0.020 & 0.020 & -0.018 \end{bmatrix}\begin{bmatrix} -0.067 - 0.119i \\ 0.069 + 0.117i \\ -0.039 - 0.059i \end{bmatrix} \\
& + \begin{bmatrix} -0.798 & 0.143 & 0.424 \\ 0.143 & -0.798 & -0.424 \\ -0.020 & 0.020 & -0.018 \end{bmatrix}\begin{bmatrix} -0.071 - 0.146i \\ -0.072 - 0.142i \\ 0.029 + 0.048i \end{bmatrix} \\
& + \begin{bmatrix} -0.798 & -0.143 & 0.424 \\ -0.143 & -0.798 & 0.424 \\ -0.020 & -0.020 & -0.018 \end{bmatrix}\begin{bmatrix} -0.063 - 0.125i \\ 0.058 + 0.123i \\ 0.027 + 0.065i \end{bmatrix} \\
& + \begin{bmatrix} -0.798 & 0.143 & -0.424 \\ 0.143 & -0.798 & 0.424 \\ 0.020 & -0.020 & -0.018 \end{bmatrix}\begin{bmatrix} -0.085 - 0.144i \\ -0.078 - 0.139i \\ -0.023 - 0.051i \end{bmatrix} \\
& + \begin{bmatrix} 1.597 & 0.500 & 0.000 \\ -0.500 & 1.597 & 0.000 \\ 0.000 & 0.000 & 0.036 \end{bmatrix}\begin{bmatrix} 0.299 + 0.485i \\ -0.153 - 0.251i \\ -0.006 - 0.002i \end{bmatrix} \\
& + \begin{bmatrix} 1.597 & -0.500 & 0.000 \\ 0.500 & 1.597 & 0.000 \\ 0.000 & 0.000 & 0.036 \end{bmatrix}\begin{bmatrix} 0.234 + 0.440i \\ 0.178 + 0.333i \\ 0.004 + 0.000i \end{bmatrix} \\
& = \boldsymbol{P}^{\boldsymbol{total}}_{\boldsymbol{x}} + \boldsymbol{P}^{\boldsymbol{total}}_{\boldsymbol{y}} + \boldsymbol{P}^{\boldsymbol{total}}_{\boldsymbol{z}} \\
& = \begin{bmatrix} 1.080 + 1.905i \\ -0.036 - 0.029i \\ -0.000 + 0.000i \end{bmatrix} + \begin{bmatrix} -0.205 - 0.367i \\ 0.060 + 0.165i \\ 0.000 - 0.000i \end{bmatrix} \\
& + \begin{bmatrix} 0.050 + 0.094i \\ 0.006 + 0.011i \\ 0.000 - 0.000i \end{bmatrix} = \begin{bmatrix} 0.925 + 1.633i \\ 0.029 + 0.147i \\ -0.000 - 0.000i \end{bmatrix} e\,\text{Å} \quad u.c.^{-1}
\end{aligned}
$$

$$
\begin{aligned}
\boldsymbol{P}(LO_5) = {} & \boldsymbol{Z}^{*}_{\boldsymbol{Bi}(1)}\boldsymbol{u}_{\mathrm{Bi}\,(1)} + \boldsymbol{Z}^{*}_{\boldsymbol{Bi}(2)}\boldsymbol{u}_{\mathrm{Bi}\,(2)} + \boldsymbol{Z}^{*}_{\boldsymbol{Bi}(3)}\boldsymbol{u}_{\mathrm{Bi}\,(3)} + \boldsymbol{Z}^{*}_{\boldsymbol{Bi}(4)}\boldsymbol{u}_{\mathrm{Bi}\,(4)} \\
& + \boldsymbol{Z}^{*}_{\boldsymbol{Sn}(1)}\boldsymbol{u}_{\mathrm{Sn}\,(1)} + \boldsymbol{Z}^{*}_{\boldsymbol{Sn}(2)}\boldsymbol{u}_{\mathrm{Sn}\,(2)} \\
= {} & \begin{bmatrix} -0.798 & -0.143 & -0.424 \\ -0.143 & -0.798 & -0.424 \\ 0.020 & 0.020 & -0.018 \end{bmatrix}\begin{bmatrix} -0.023 + 0.090i \\ -0.001 + 0.011i \\ 0.037 - 0.168i \end{bmatrix} \\
& + \begin{bmatrix} -0.798 & 0.143 & 0.424 \\ 0.143 & -0.798 & -0.424 \\ -0.020 & 0.020 & -0.018 \end{bmatrix}\begin{bmatrix} -0.027 + 0.085i \\ -0.003 + 0.009i \\ -0.038 + 0.124i \end{bmatrix} \\
& + \begin{bmatrix} -0.798 & -0.143 & 0.424 \\ -0.143 & -0.798 & 0.424 \\ -0.020 & -0.020 & -0.018 \end{bmatrix}\begin{bmatrix} -0.023 + 0.094i \\ -0.004 + 0.009i \\ -0.047 + 0.165i \end{bmatrix} \\
& + \begin{bmatrix} -0.798 & 0.143 & -0.424 \\ 0.143 & -0.798 & 0.424 \\ 0.020 & -0.020 & -0.018 \end{bmatrix}\begin{bmatrix} -0.018 + 0.092i \\ 0.001 + 0.011i \\ 0.028 - 0.128i \end{bmatrix} \\
& + \begin{bmatrix} 1.597 & 0.500 & 0.000 \\ -0.500 & 1.597 & 0.000 \\ 0.000 & 0.000 & 0.036 \end{bmatrix}\begin{bmatrix} 0.048 - 0.243i \\ 0.112 - 0.591i \\ -0.011 + 0.005i \end{bmatrix} \\
& + \begin{bmatrix} 1.597 & -0.500 & 0.000 \\ 0.500 & 1.597 & 0.000 \\ 0.000 & 0.000 & 0.036 \end{bmatrix}\begin{bmatrix} 0.099 - 0.396i \\ -0.132 + 0.514i \\ 0.012 + 0.000i \end{bmatrix} \\
= {} & \boldsymbol{P}^{\boldsymbol{total}}_{\boldsymbol{x}} + \boldsymbol{P}^{\boldsymbol{total}}_{\boldsymbol{y}} + \boldsymbol{P}^{\boldsymbol{total}}_{\boldsymbol{z}} \\
= {} & \begin{bmatrix} 0.307 - 1.310i \\ -0.026 - 0.077i \\ 0.000 + 0.000i \end{bmatrix} + \begin{bmatrix} 0.122 - 0.552i \\ -0.026 - 0.155i \\ 0.000 + 0.000i \end{bmatrix} \\
& + \begin{bmatrix} -0.063 + 0.248i \\ -0.008 + 0.035i \\ 0.000 + 0.000i \end{bmatrix} = \begin{bmatrix} 0.366 - 1.614i \\ -0.008 - 0.198i \\ 0.001 + 0.000i \end{bmatrix} e\,\text{Å} \quad u.c.^{-1}
\end{aligned}
$$

$$
\begin{aligned}
\boldsymbol{P}(LO_1) &= \boldsymbol{Z}^{*}_{\boldsymbol{Bi}(\mathbf{1})}\boldsymbol{u}_{\mathrm{Bi}\,(\mathbf{1})} + \boldsymbol{Z}^{*}_{\boldsymbol{Bi}(\mathbf{2})}\boldsymbol{u}_{\mathrm{Bi}\,(\mathbf{2})} + \boldsymbol{Z}^{*}_{\boldsymbol{Bi}(\mathbf{3})}\boldsymbol{u}_{\mathrm{Bi}\,(\mathbf{3})} + \boldsymbol{Z}^{*}_{\boldsymbol{Bi}(\mathbf{4})}\boldsymbol{u}_{\mathrm{Bi}\,(\mathbf{4})} \\
&\quad + \boldsymbol{Z}^{*}_{\boldsymbol{Sn}(\mathbf{1})}\boldsymbol{u}_{\mathrm{Sn}\,(\mathbf{1})} + \boldsymbol{Z}^{*}_{\boldsymbol{Sn}(\mathbf{2})}\boldsymbol{u}_{\mathrm{Sn}\,(\mathbf{2})} \\
&= \begin{bmatrix} -0.798 & -0.143 & -0.424 \\ -0.143 & -0.798 & -0.424 \\ 0.020 & 0.020 & -0.018 \end{bmatrix}\begin{bmatrix} -0.029 - 0.411i \\ -0.023 - 0.228i \\ -0.005 + 0.123i \end{bmatrix} \\
&\quad + \begin{bmatrix} -0.798 & 0.143 & 0.424 \\ 0.143 & -0.798 & -0.424 \\ -0.020 & 0.020 & -0.018 \end{bmatrix}\begin{bmatrix} 0.010 + 0.361i \\ -0.013 + 0.111i \\ -0.010 + 0.048i \end{bmatrix} \\
&\quad + \begin{bmatrix} -0.798 & -0.143 & 0.424 \\ -0.143 & -0.798 & 0.424 \\ -0.020 & -0.020 & -0.018 \end{bmatrix}\begin{bmatrix} -0.001 - 0.412i \\ 0.027 - 0.229i \\ -0.010 - 0.122i \end{bmatrix} \\
&\quad + \begin{bmatrix} -0.798 & 0.143 & -0.424 \\ 0.143 & -0.798 & 0.424 \\ 0.020 & -0.020 & -0.018 \end{bmatrix}\begin{bmatrix} 0.023 + 0.360i \\ -0.002 + 0.110i \\ -0.020 - 0.047i \end{bmatrix} \\
&\quad + \begin{bmatrix} 1.597 & 0.500 & 0.000 \\ -0.500 & 1.597 & 0.000 \\ 0.000 & 0.000 & 0.036 \end{bmatrix}\begin{bmatrix} 0.027 + 0.323i \\ 0.018 + 0.105i \\ 0.001 + 0.000i \end{bmatrix} \\
&\quad + \begin{bmatrix} 1.597 & -0.500 & 0.000 \\ 0.500 & 1.597 & 0.000 \\ 0.000 & 0.000 & 0.036 \end{bmatrix}\begin{bmatrix} -0.012 - 0.140i \\ 0.005 + 0.312i \\ -0.008 + 0.000i \end{bmatrix} \\
&= \boldsymbol{P}^{\boldsymbol{total}}_{\boldsymbol{x}} + \boldsymbol{P}^{\boldsymbol{total}}_{\boldsymbol{y}} + \boldsymbol{P}^{\boldsymbol{total}}_{\boldsymbol{z}} \\
&= \begin{bmatrix} 0.022 + 0.374i \\ -0.011 - 0.011i \\ -0.000 + 0.000i \end{bmatrix} + \begin{bmatrix} 0.004 - 0.006i \\ 0.046 + 0.854i \\ -0.001 + 0.000i \end{bmatrix} \\
&\quad + \begin{bmatrix} 0.002 - 0.064i \\ -0.006 - 0.144i \\ 0.001 - 0.000i \end{bmatrix} = \begin{bmatrix} 0.028 + 0.304i \\ 0.029 + 0.699i \\ -0.001 - 0.000i \end{bmatrix} e\ \text{Å} \quad u.c.^{-1}
\end{aligned}
$$

$$
\begin{aligned}
\boldsymbol{P}(LO_2) &= \boldsymbol{Z}^{*}_{\boldsymbol{Bi(1)}}\boldsymbol{u}_{\mathrm{Bi\,(1)}} + \boldsymbol{Z}^{*}_{\boldsymbol{Bi(2)}}\boldsymbol{u}_{\mathrm{Bi\,(2)}} + \boldsymbol{Z}^{*}_{\boldsymbol{Bi(3)}}\boldsymbol{u}_{\mathrm{Bi\,(3)}} + \boldsymbol{Z}^{*}_{\boldsymbol{Bi(4)}}\boldsymbol{u}_{\mathrm{Bi\,(4)}} \\
&\quad + \boldsymbol{Z}^{*}_{\boldsymbol{Sn(1)}}\boldsymbol{u}_{\mathrm{Sn\,(1)}} + \boldsymbol{Z}^{*}_{\boldsymbol{Sn(2)}}\boldsymbol{u}_{\mathrm{Sn\,(2)}} \\
&= \begin{bmatrix} -0.798 & -0.143 & -0.424 \\ -0.143 & -0.798 & -0.424 \\ 0.020 & 0.020 & -0.018 \end{bmatrix} \begin{bmatrix} -0.342 - 0.049i \\ -0.341 - 0.042i \\ 0.114 + 0.018i \end{bmatrix} \\
&\quad + \begin{bmatrix} -0.798 & 0.143 & 0.424 \\ 0.143 & -0.798 & -0.424 \\ -0.020 & 0.020 & -0.018 \end{bmatrix} \begin{bmatrix} -0.338 - 0.070i \\ 0.337 + 0.063i \\ -0.113 - 0.025i \end{bmatrix} \\
&\quad + \begin{bmatrix} -0.798 & -0.143 & 0.424 \\ -0.143 & -0.798 & 0.424 \\ -0.020 & -0.020 & -0.018 \end{bmatrix} \begin{bmatrix} 0.334 + 0.082i \\ 0.334 + 0.089i \\ 0.110 + 0.025i \end{bmatrix} \\
&\quad + \begin{bmatrix} -0.798 & 0.143 & -0.424 \\ 0.143 & -0.798 & 0.424 \\ 0.020 & -0.020 & -0.018 \end{bmatrix} \begin{bmatrix} 0.338 + 0.060i \\ -0.339 - 0.067i \\ -0.112 - 0.018i \end{bmatrix} \\
&\quad + \begin{bmatrix} 1.597 & 0.500 & 0.000 \\ -0.500 & 1.597 & 0.000 \\ 0.000 & 0.000 & 0.036 \end{bmatrix} \begin{bmatrix} 0.002 + 0.007i \\ 0.000 + 0.004i \\ 0.001 + 0.000i \end{bmatrix} \\
&\quad + \begin{bmatrix} 1.597 & -0.500 & 0.000 \\ 0.500 & 1.597 & 0.000 \\ 0.000 & 0.000 & 0.036 \end{bmatrix} \begin{bmatrix} 0.001 + 0.007i \\ 0.001 - 0.004i \\ -0.000 + 0.000i \end{bmatrix} \\
&= \boldsymbol{P}^{\boldsymbol{total}}_{\boldsymbol{x}} + \boldsymbol{P}^{\boldsymbol{total}}_{\boldsymbol{y}} + \boldsymbol{P}^{\boldsymbol{total}}_{\boldsymbol{z}} \\
&= \begin{bmatrix} 0.011 + 0.004i \\ 0.001 - 0.006i \\ 0.000 + 0.000i \end{bmatrix} + \begin{bmatrix} 0.001 - 0.003i \\ 0.008 - 0.034i \\ 0.000 - 0.000i \end{bmatrix} \\
&\quad + \begin{bmatrix} -0.002 - 0.000i \\ -0.001 + 0.006i \\ 0.000 + 0.000i \end{bmatrix} = \begin{bmatrix} 0.010 + 0.001i \\ 0.008 - 0.034i \\ 0.000 + 0.000i \end{bmatrix} e\,\text{Å} \quad u.c.^{-1}
\end{aligned}
$$

APPENDIX IV

Thermoelectric Properties at 300 K, 550 K and 700 K

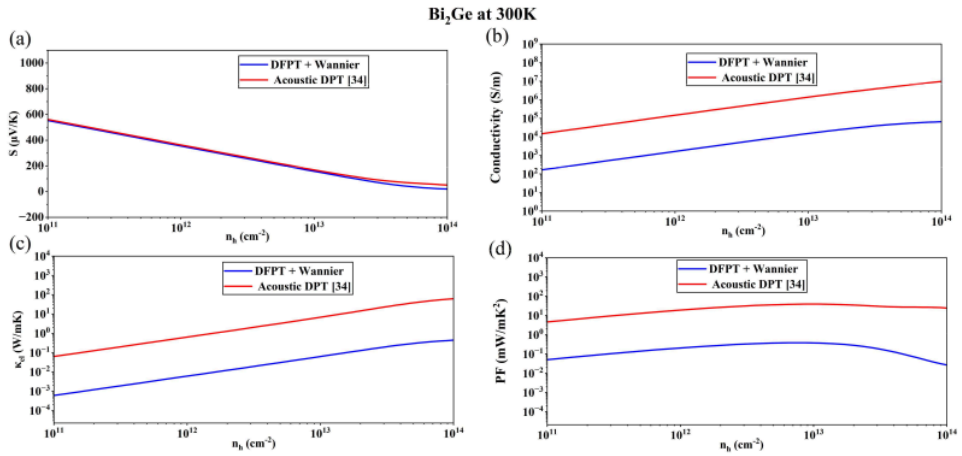

Fig. A IV.1 Thermoelectric transport coefficients of p-type Bi_2Ge plotted against extrinsic hole concentration (n_h) at 300K. The carrier relaxation time for Acoustic DPT calculation were taken from Lv et al [34]

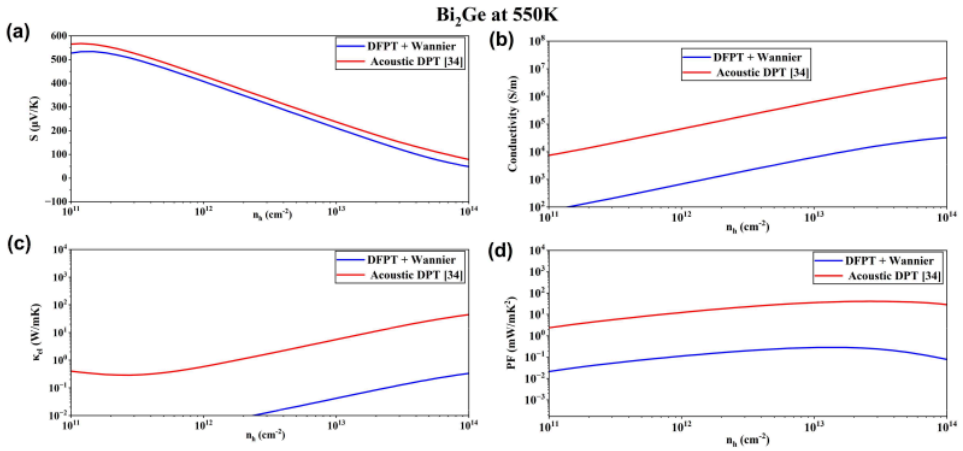

Fig. A IV.2 Thermoelectric transport coefficients of p-type Bi_2Ge plotted against extrinsic hole concentration $(\boldsymbol{n_h})$ at 550K. The carrier relaxation time for Acoustic DPT calculation were taken from Lv et al [34]

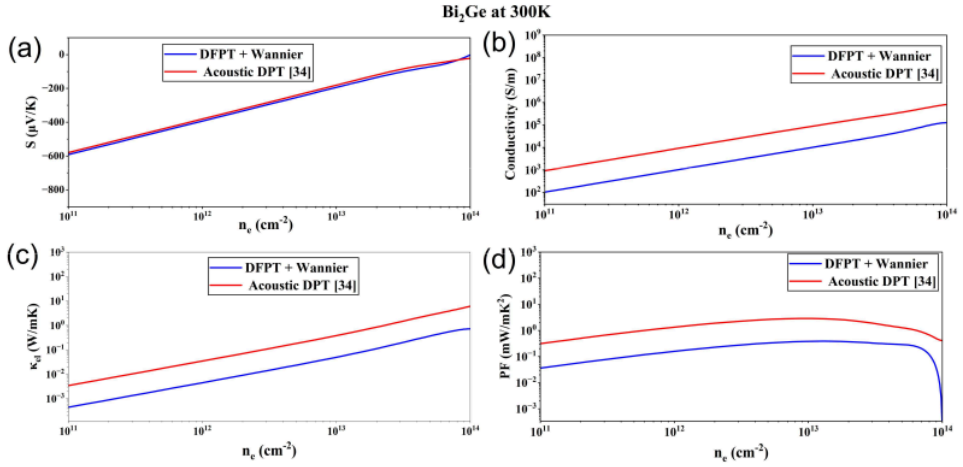

Fig. A IV.3 Thermoelectric transport coefficients of n-type Bi_2Ge plotted against extrinsic electron concentration $(\boldsymbol{n_e})$ at 300K. The carrier relaxation time for Acoustic DPT calculation were taken from Lv et al [34]

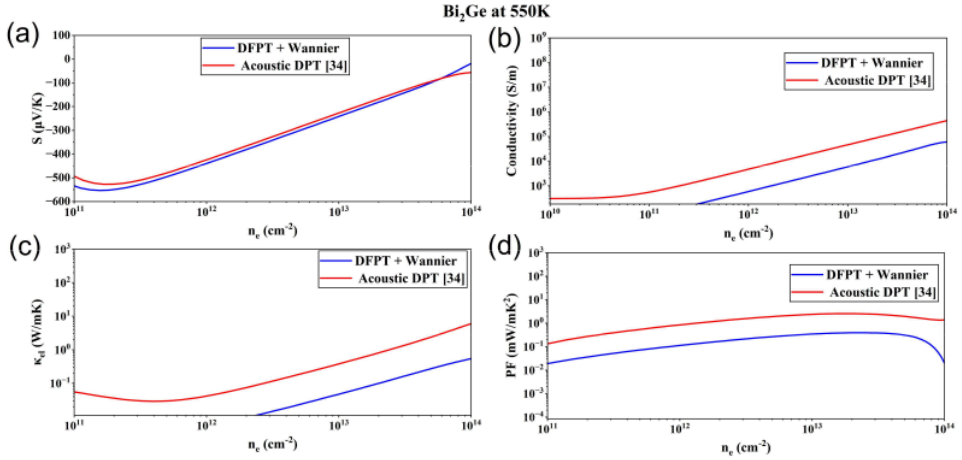

Fig. A IV.4 Thermoelectric transport coefficients of n-type Bi_2Ge plotted against extrinsic electron concentration $(\boldsymbol{n_e})$ at 300K. The carrier relaxation time for Acoustic DPT calculation were taken from Lv et al [34]

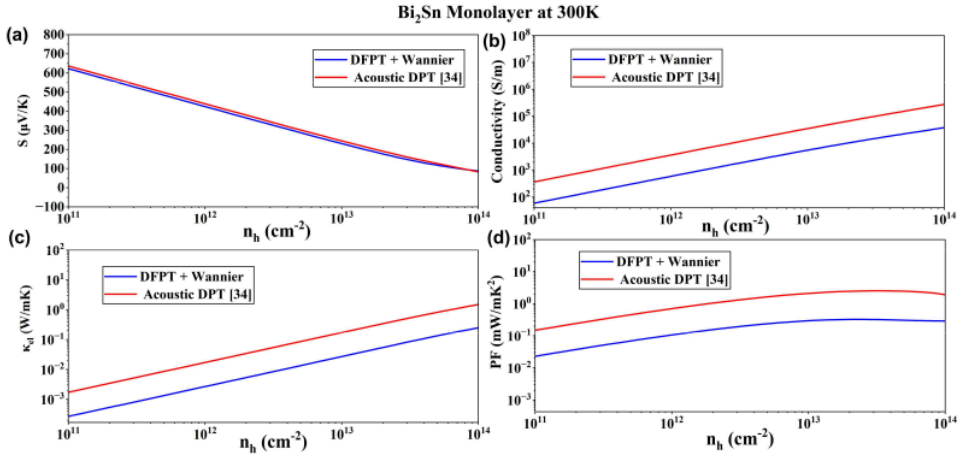

Fig. A IV.5 Thermoelectric transport coefficients of p-type Bi_2Sn plotted against extrinsic hole concentration $(\boldsymbol{n_h})$ at 300K. The carrier relaxation time for Acoustic DPT calculation were taken from Lv et al [34]

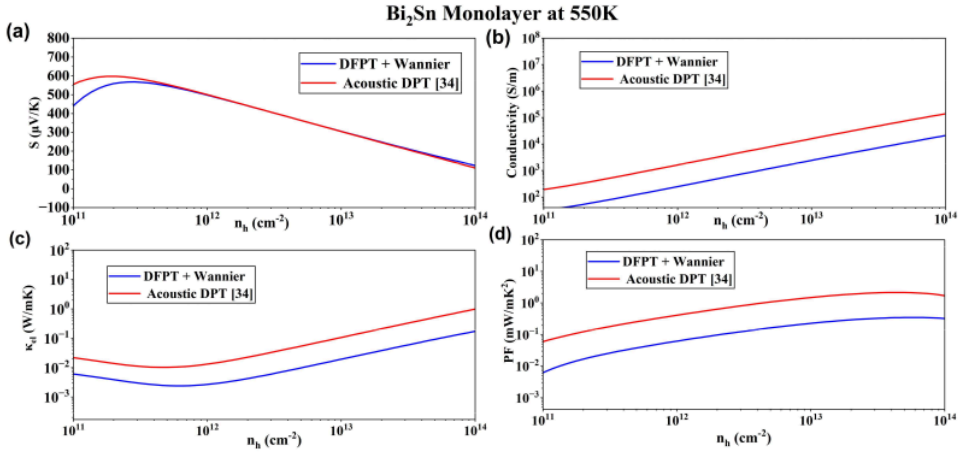

Fig. A IV.6 Thermoelectric transport coefficients of p-type Bi_2Sn plotted against extrinsic hole concentration $(\boldsymbol{n_h})$ at 550K. The carrier relaxation time for Acoustic DPT calculation were taken from Lv et al [34]

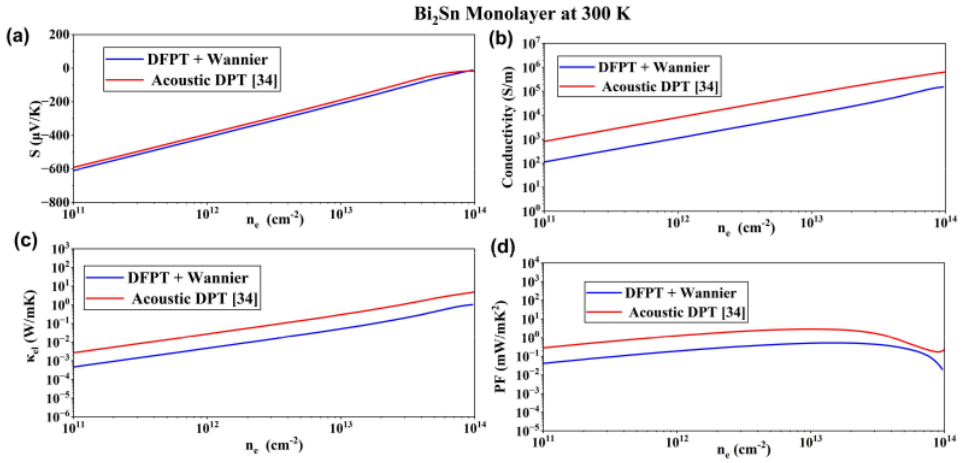

Fig. A IV.7 Thermoelectric transport coefficients of n-type Bi_2Sn plotted against extrinsic electron concentration $(\boldsymbol{n_e})$ at 300K. The carrier relaxation time for Acoustic DPT calculation were taken from Lv et al [34]

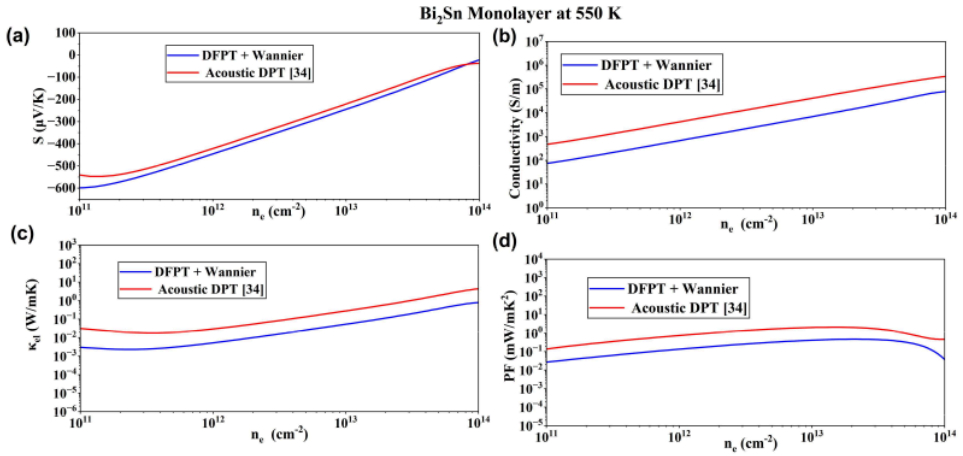

Fig. A IV.8 Thermoelectric transport coefficients of n-type Bi_2Sn plotted against extrinsic electron concentration (n_e) at 550K. The carrier relaxation time for Acoustic DPT calculation were taken from Lv et al [34]

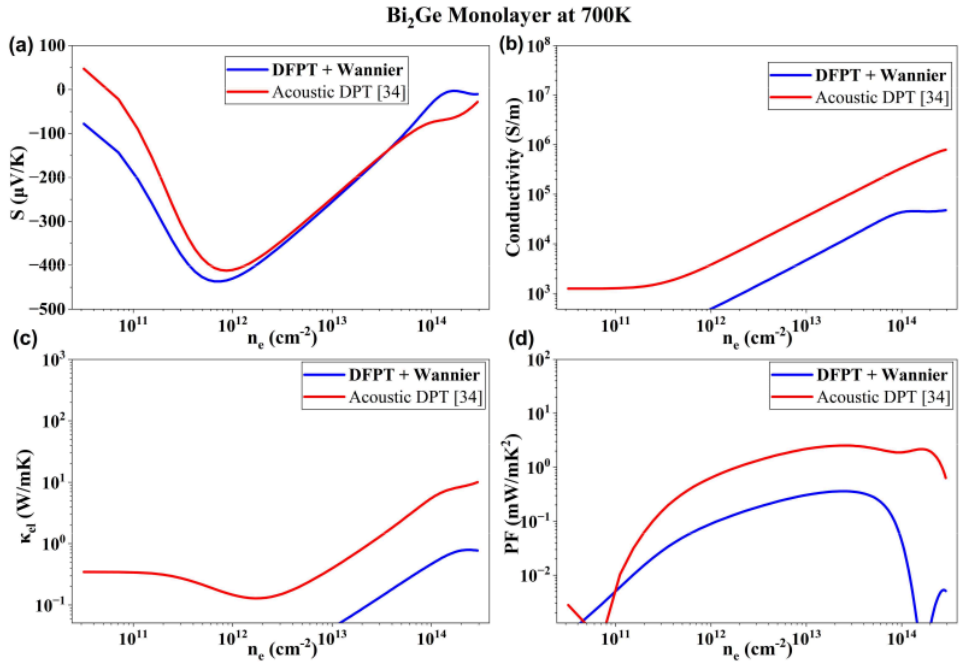

Fig. A IV.9 Thermoelectric transport coefficients of n-type Bi_2Ge plotted against extrinsic electron concentration (n_e) at 700K. The carrier relaxation time for Acoustic DPT calculation were taken from Lv et al [34]

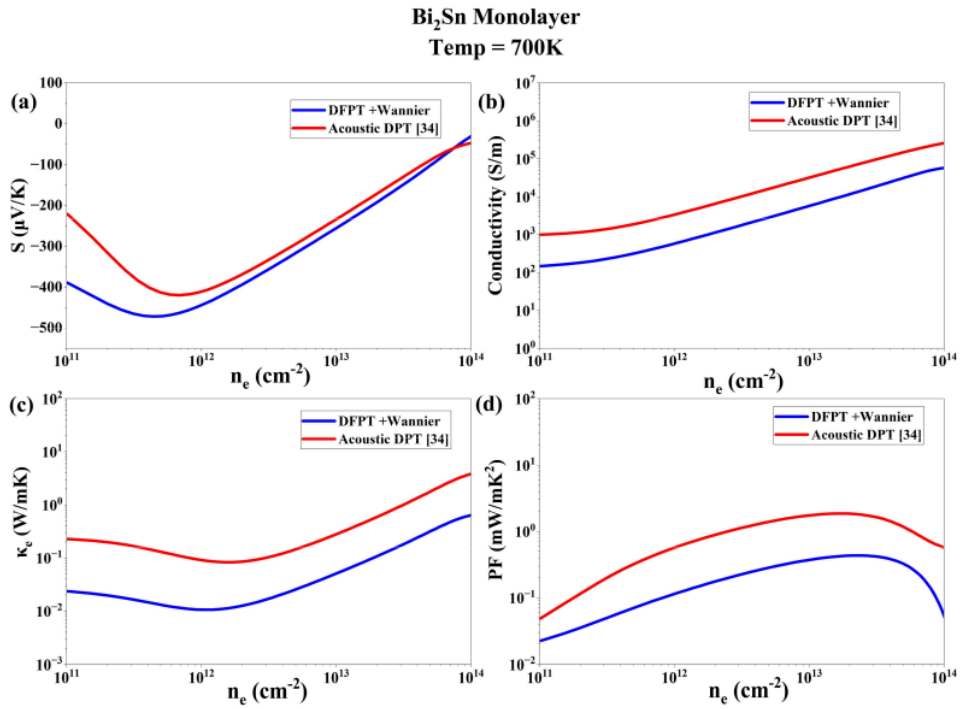

Fig. A IV.10. Thermoelectric transport coefficients of p-type Bi_2Sn plotted against extrinsic electron concentration (n_e) at 700K: **(a)** *S*, **(b)** σ, **(c)** κ_e, and **(d)** PF = $S^2\sigma$. The carrier relaxation time for Acoustic DPT calculation were taken from Lv et al [34]

MSc-ma

ORIGINALITY REPORT

9%	4%	7%	4%
SIMILARITY INDEX	INTERNET SOURCES	PUBLICATIONS	STUDENT PAPERS

PRIMARY SOURCES

1	www.il-pib.pl Internet Source	1%
2	K. Adcox. "Single identified hadron spectra from sqrt[s_{NN}]=130GeV Au+Au collisions", Physical Review C, 02/2004 Publication	1%
3	Te-Huan Liu, Bai Song, Laureen Meroueh, Zhiwei Ding, Qichen Song, Jiawei Zhou, Mingda Li, Gang Chen. "Simultaneously high electron and hole mobilities in cubic boron-V compounds: BP, BAs, and BSb", Physical Review B, 2018 Publication	1%
4	arxiv.org Internet Source	1%
5	Advanced Texts in Physics, 2003. Publication	1%
6	Yule Mayevsky, Akram Youssry, Ritik Sareen, Gerardo A. Paz-Silva, Alberto Peruzzo. "Quantum engineering of qudits with interpretable machine learning", Quantum Machine Intelligence, 2026	<1%

Publication

7	Ponomareva Olga, Ponomarev Alexey, Smirnova Natalia. "Complex-Conjugate Symmetry of Coefficients of Two-Dimensional Discrete Fourier Transform with Variable Parameters of Real Signals", 2022 24th International Conference on Digital Signal Processing and its Applications (DSPA), 2022 Publication	<1 %
8	Yu-Lu Wan, Qiu Yang, Tian Zhang, Zhao-Yi Zeng, Xiang-Rong Chen. "High thermoelectric performance in Ti2OX2 (X = F, Cl) MOene: A first-principles study incorporating electron–phonon coupling", Journal of Applied Physics, 2024 Publication	<1 %
9	Halid Bikkin, Igor I. Lyapilin. "Non-equilibrium thermodynamics and physical kinetics", Walter de Gruyter GmbH, 2014 Publication	<1 %
10	Weng Hong Sio, Feliciano Giustino. " Unified description of Fröhlich electron-phonon interactions in two-dimensional and three-dimensional materials ", Physical Review B, 2022 Publication	<1 %
11	Robert A. Evarestov. "Quantum Chemistry of Solids", Springer Science and Business Media LLC, 2012 Publication	<1 %

12	Submitted to University of Hong Kong Student Paper	<1%
13	Maud Einhorn, Benjamin A. D. Williamson, David O Scanlon. "Computational Prediction of the Thermoelectric Performance of LaZnOPn (Pn = P, As)", Journal of Materials Chemistry A, 2020 Publication	<1%
14	Submitted to University of Witwatersrand Student Paper	<1%
15	exchangetuts.com Internet Source	<1%
16	tel.archives-ouvertes.fr Internet Source	<1%
17	Meng-Yuan Yu, Chuan-Lu Yang, Xiaohu Li, Yuliang Liu, Wenkai Zhao, Feng Gao. "Ultralow lattice thermal conductivity and exceptional thermoelectric performance in the YbBi2 monolayer induced by strong four-phonon scattering", Materials Research Bulletin, 2026 Publication	<1%
18	Submitted to Trinity College Dublin Student Paper	<1%
19	Submitted to University of Cambridge Student Paper	<1%
20	d-nb.info Internet Source	<1%

21	Peter Y. Yu, Manuel Cardona. "Fundamentals of Semiconductors", Springer Science and Business Media LLC, 2010 Publication	<1 %
22	Relativistic Methods for Chemists, 2010. Publication	<1 %
23	Samuel Poncé, Francesco Macheda, Elena Roxana Margine, Nicola Marzari, Nicola Bonini, Feliciano Giustino. "First-principles predictions of Hall and drift mobilities in semiconductors", Physical Review Research, 2021 Publication	<1 %
24	Torkia Ghellab, Hakim Baaziz, Zoulikha Charifi. "Tailoring the physical characteristics of novel quaternary RuMnCrSi and NiMnCrAl compounds for spintronic and thermoelectric applications", Physica Scripta, 2025 Publication	<1 %
25	Zhang, Zhen. "Phonon Quasiparticle Studies of Anharmonic Properties of Solids", Columbia University, 2023 Publication	<1 %
26	Submitted to Coventry University Student Paper	<1 %
27	Luis A. Agapito, Marco Bernardi. " electron-phonon interactions using atomic orbital wave functions ", Physical Review B, 2018 Publication	<1 %

28	Ying Chen, Yu Wu, Bowen Hou, Jiang Cao, Hezhu Shao, Yiming Zhang, Haodong Mei, Congcong Ma, Zhilai Fang, Heyuan Zhu, Hao Zhang. " Renormalized thermoelectric figure of merit in band-convergent Sb Te Se monolayer: full electron-phonon interactions and selection rules ", Journal of Materials Chemistry A, 2021 Publication	<1 %
29	Submitted to University of Lincoln Student Paper	<1 %
30	Submitted to Imperial College of Science, Technology and Medicine Student Paper	<1 %
31	Kazutoshi Miwa. "Prediction of Raman spectra with ultrasoft pseudopotentials", Physical Review B, 2011 Publication	<1 %
32	Ming-Gang Ju, Min Chen, Yuanyuan Zhou, Hector F. Garces, Jun Dai, Liang Ma, Nitin P. Padture, Xiao Cheng Zeng. "Earth-Abundant Nontoxic Titanium(IV)-based Vacancy-Ordered Double Perovskite Halides with Tunable 1.0 to 1.8 eV Bandgaps for Photovoltaic Applications", ACS Energy Letters, 2018 Publication	<1 %
33	Submitted to Nanyang Technological University, Singapore Student Paper	<1 %

34	Ouyang, Chien, Kenny Gross, and Ali Heydari. "Hot Spot Cooling Using Recycled Energy", ASME 2007 InterPACK Conference Volume 2, 2007. Publication	<1%
35	Submitted to University of Leeds Student Paper	<1%
36	assets-eu.researchsquare.com Internet Source	<1%
37	Rakib, Tawfiqur. "Coupling of Deformation and Electronic Properties in Two-Dimensional Materials", University of Illinois at Urbana-Champaign Publication	<1%
38	Vasileska, . "Semiclassical Transport Theory", Computational Electronics Semiclassical and Quantum Device Modeling and Simulation, 2010. Publication	<1%
39	Huang, Zuocai, Lei Zhang, and Wei Pan. "Physical properties of zircon and scheelite lutetium orthovanadate: Experiment and first-principles calculation", Journal of Solid State Chemistry, 2013. Publication	<1%
40	iopscience.iop.org Internet Source	<1%

Exclude quotes	Off	Exclude matches	< 10 words
Exclude bibliography	Off		